Aero-elastic Energy Harvesting Device:
Design and Analysis

by

Oliver Johann Pirquet
B Eng, University of Victoria, 2012

A Thesis Submitted in Partial Fulfillment
of the Requirements for the Degree of

MASTER OF APPLIED SCIENCE

in the Department of Mechanical Engineering

Supervisory Committee

Aero-elastic energy harvesting device:
Design and analysis

by

Oliver Johann Pirquet
B Eng, University of Victoria, 2012

Supervisory Committee

Dr. Ben Nadler (Department of Mechanical Engineering)
Supervisor

Dr. Curran Crawford (Department of Mechanical Engineering)
Co-Supervisor

Abstract

Dr. Ben Nadler (Department of Mechanical Engineering)
Supervisor

Dr. Curran Crawford (Department of Mechanical Engineering)
Co-Supervisor

An energy harvesting device driven by aeroelastic vibration with self-sustained pitching and heaving using an induction based power take off mechanism has been designed and tested for performance under various operating conditions. From the data collected the results show that the device achieved a maximum power output of 48.3 mW and a maximum efficiency of 2.26% at a dimensionless frequency of 0.143. For all airfoils tested the device was shown to be self-starting above 3 m/s. A qualitative description relating to the performance of the device considering dynamic stall and the flow conditions at optimal dimensionless frequency has been proposed and related to previous work. Performance for angles off the wind up to 22 degrees and was observed to have no reduction in power output due to the change in angle to the wind. The device has shown evidence of having a self-governing capability, tending to decrease its power output for heavy windpspeeds, a thorough examination of this capability is recommended for future work.

Table of Contents

List of Tables

List of Figures

Acknowledgments

I would like to acknowledge:

My mother and father for bringing me into this world, without them I and this thesis would not exist. My supervisors Drs. Ben Nadler and Curran Crawford for taking me on as a master student and their advice and aid throughout the process. The gracious help of a Mr. Ted White at Novaculture Inc. for helping with design formulation, construction of prototype and testing equipment, and taking me on for the NSERC IPS (Industrial Partner Sponsor) grant. NSERC for their contributions to my financial needs throughout the first two years of this investigation. Mr. Nik Zapantis from the Physics department who allowed me to use equipment and space during the device testing portion of the investigation. Dr. Alex Van Netten from the physics department for agreeing to act as the external examiner for my oral examination. Mr. Arthur Makosinski for being so helpful with equipment and letting me use the wind tunnel in the fluids lab at all hours of the day and night. Mr. Patrick Chang for letting me use equipment and ask him questions. My office mates, group members at EISVic, friends and family, and anyone I forgot, thank you so much!

Dedication

I would like to dedicate this thesis to Mrs. June P Kern. She a scholar, an artist, and one of the most courageous woman I know. She has always been a source of inspiration in my life. I am truly blessed to have such a remarkable woman for a grandmother.

Chapter 1: Introduction

Elastic structures immersed in moving fluids often undergo flow-induced vibration of some kind. In most situations this effect is seen as a detriment as it leads to vibration of components and structures, causing them to fatigue and sometimes fail. The well-known example of the Tacoma Narrows bridge collapse, which resulted in catastrophic failure of a suspension bridge due to vibration induced by a harmonic coupling between the bridge structure and the aerodynamic forces on the bridge surface (fig. 1) illustrates the scale of these effects and the need to account for them in design. For this reason much of the research dedicated to flow-induced vibration has been focussed on the effort either to mitigate the effect or to prevent it. Studies of flow-induced vibration have allowed scientists and engineers to understand the system properties, fluid flow and structural, that produces and influence flow-induced vibration, and to use that understanding to design structures that can either handle the vibration or reduce its negative effects (helical additions to columns, splitter plates, and filaments [1]).

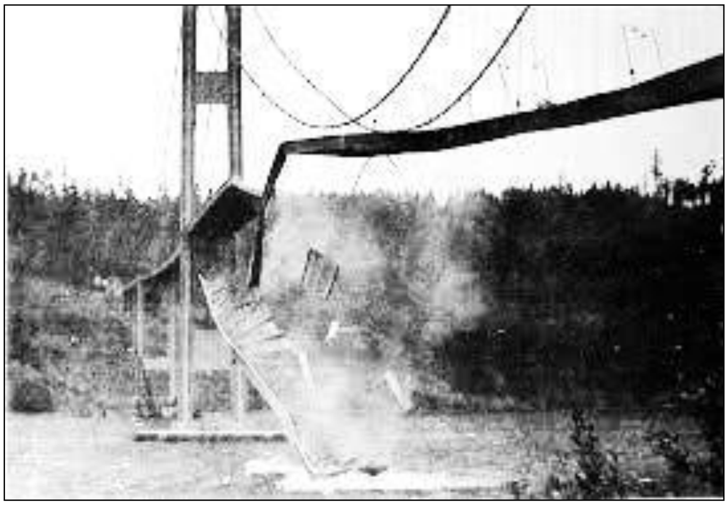

Figure 1 Tacoma narrows bridge collapse [37]

Recently, largely within the last 15 years, the need for devices that “harvest” energy from ambient energy sources has accelerated, due to increasing use of low-power monitoring devices (temperature, strain, chemical composition, etc.) in locations that are difficult to service. Harvesting energy means that the power needed for a device or service can be “harvested” from the local environment. This reduces or eliminates the need to change batteries (a task that could be impossible in some locations). For devices in environments that are subject to ambient fluid flow, there exists the potential to couple a device undergoing flow induced vibration with a power take-off mechanism; in this case flow-induced vibration is used to generate the electric power needed to operate the device or charge batteries. Fluid flow powered energy harvesting devices are typically low power, on the order of milli Watts and due to their small size, with characteristic lengths of less than 10 cm. They also operate at reduced efficiencies compared to large scale turbines which have improved efficiencies due to their large aspect ratios and size relative to flow instabilities. For the purposes of understanding the energy harvester design and analysis presented in this thesis, the literature review, chapter 1, will survey investigations of structural vibration caused by flutter and vortex shedding, and investigate electric generators developed using those phenomena.

1.1 Flutter

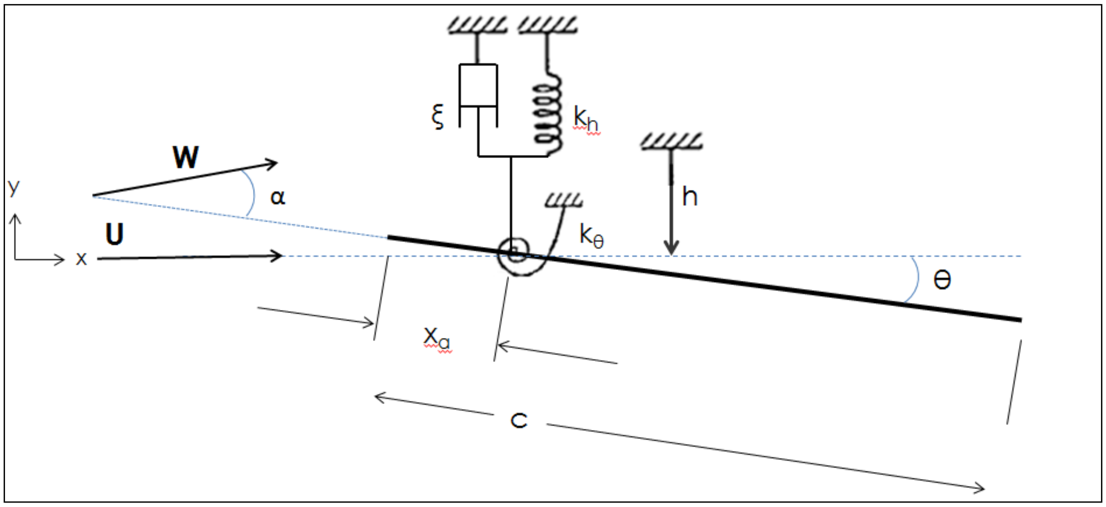

Figure 2 Typical foil cross section and relevant parameters

Referring to figure 2 (showing a cross section of the typical geometry, in this case the foil is pictured as a flat plate, although in general it can take any shape), where h is the heaving displacement, α is the angle of attack to the relative wind speed W (note: the relative wind speed is not constant over the whole foil due to its motion in rotation and displacement). The angular rotation relative to the global averaged wind direction U is given by θ. k_h is the heaving stiffness, k_θ is the torsion stiffness, the combined damping of the system in the heave orientation including the power take off is given by ξ_h, c is the chord length and the parameter x_a is the distance from the leading edge to the airfoil axis of rotation. In general, there would be damping in the torsional axis of the foil, ξ_Θ , though it is not shown in this diagram. Classical flutter is described here as a phenomenon that occurs when a stiff airfoil (stiff: does not bend appreciably along the chord)~~,~~ in a moving fluid, having the freedom to move in twist about z and heave along y directions, and having stiffness in one or both degrees of freedom, undergoes a limit cycle oscillation which is at least self-sustaining for a given flow speed and damping condition. It is important to note that for a fluttering system without damping or some kind of physical limit of motion, the amplitude is indeterminate, or divergent. This can be seen in a 1 degree of freedom forced elastic systems with no damping where the forcing frequency (caused by the pitch degree of freedom interacting with the flow, this case considers prescribed motion of the pitch degree of freedom leading to the equation of motion for forced heave) is equal to the natural frequency heave vibration.

$$M\ddot{h} + \xi_h \dot{h} + k_h h = F(t), \tag{1.1}$$

where M is the equivalent mass of the system and considering

$$F(t) = A\sin(\omega_n t + \phi), \tag{1.2}$$

where A is the non-zero amplitude of the forcing function and ω_n is the natural frequency of the homogeneous solution, the solution for $h(t)$ becomes divergent for damping ξ_h , approaching zero.

Flutter occurs, for most systems, at a particular flow speed, U, for a given system; this is known as the critical flutter velocity, V_c. In Theodorsen's description of flutter [2], this is described as the divergence velocity, which is the operating point where the drag forces on an airfoil that would critically damp out perturbations in the torsion and heave directions are overcome by the dynamic forces leading to flutter. Theodorsen's description is mostly concerned with this critical condition; at the outset of his seminal paper he describes the motions of concern to be of "infinitesimally small oscillations", this being the condition existing at flutter onset.

1.1.1 Quasi-steady description of flutter

It is useful to understand a (quasi-steady) qualitative first approximation of flutter by considering the mechanisms of flight involved. The phase relationship between heave and angular displacement of the foil exhibit two possible extremum states [3], as shown in figure 3. In the first case, there is a 90 degree phase relationship between the pitch and heave motions. This phase difference, considering a moving fluid over an airfoil, results in lift on the airfoil which is in the same direction of heave motion throughout a whole cycle of oscillation. This condition results in work done over a cycle. In the second case the lift force alternates with and against the motion resulting in no work done over a cycle. Both cases are modeled by the equation of work which states that

$$\delta W = F \cdot ds, \tag{1.3}$$

where δW is the element of work done by the Force F acting allong the differential path element ds. This relationship can be integrated over the path of one oscillation to determine the total work done per cycle of motion.

This description is illustrative in that we have two different phase relationships of operation which describe an all-or-nothing potential for power generation in the motion of the foil. This is a quasi-steady analysis and the assumption of reciprocity between the up and down motions as being equal and opposite in force direction and magnitude is not accounting for unsteady flow interactions, although it does provide a model to understand the importance of lift direction and the phase relationship between pitch angle and heave in flutter.

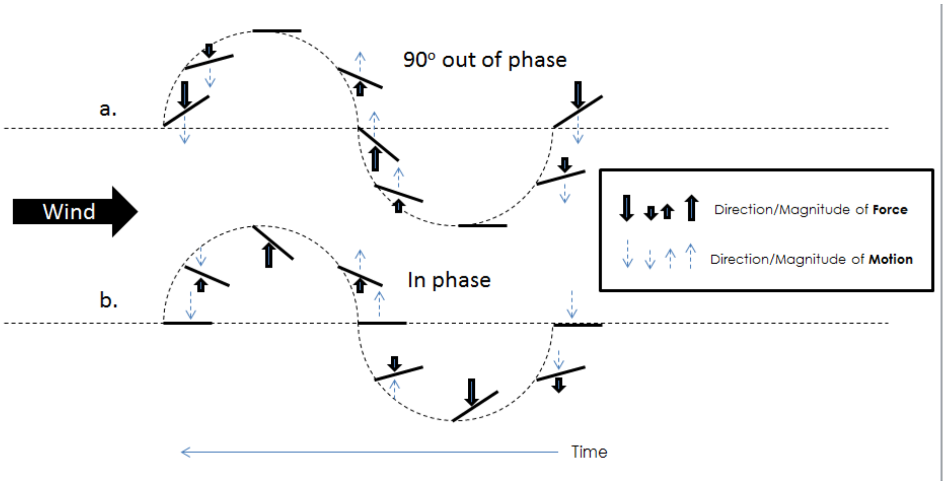

Figure 3 Quasi steady phase relationship diagrams, a. 90°- positive work over a cycle of motion, b. 0°- no work done over a cycle

1.1.2 Theodorsen Function

For quazi-steady flow analysis the vorticity leaving the trailing edge of a foil is considered negligible (vorticity convected or 'shed' downstream does not affect the lift on the air foil). For scenarios that create a wake, such as in flutter, this assumption is no longer valid, so there is a need to consider the losses involved in shedding of the wake downstream. Theodorsen [2] generated a function that effectively reduces the lift developed over the foil corresponding to unsteady flow in the wake. The formulation is derived using potential flow functions describing the foil and wake in terms of source vortices and sinks which are mapped onto a flat plate using a Joukowski conformal transformation. The derivation of the differential equation describing the lift and moment over the foil is extensive and is not shown here; rather, the results are provided for consideration.

Theodorsen’s total lift involves the addition of both the circulatory and non-circulatory lift shown as

$$l = l_{nc} + l_c = \rho \pi b^2 \left(\ddot{h} - \left(x_a - \frac{c}{2}\right)\ddot{\theta} + U\dot{\theta}\right) + \pi \rho U c C \quad (1.4)$$

$$\left(U\theta + \dot{h} + \left(\tfrac{3c}{4} - x_a\right)\dot{\theta}\right),$$

and similarly the moment over the foil is given as

$$m = m_{nc} + m_c = \rho \pi b^2 \left(x_f - \frac{c}{2}\right)\left(h - \left(x_f - \frac{c}{2}\right)\ddot{\theta}\right) - \frac{\rho \pi b^4}{8}\ddot{\theta} - \rho \pi b^2 \quad (1.5)$$

$$\left(\tfrac{3c}{4} - x_a\right)\dot{\theta} + \pi \rho U e c^2 C \left(U\theta + \dot{h} + \left(\tfrac{3c}{4} - x_a\right)\dot{\theta}\right),$$

where l_{nc} and l_c are the non-circulatory and circulatory lift respectively, ρ is density of the fluid, b is the half-chord length of chord *c*, and x_a is the chord-wise distance from the leading edge of the foil to the center of rotation for θ. m_{nc} and m_c are the non-circulatory and circulatory moments, respectively. A “practical” approximation for *C* is given by

$$C = 1 - \frac{0.165}{1 - \frac{0.0455}{k}j} - \frac{0.335}{1 - \frac{0.3}{k}j}, \quad (1.6)$$

where k is the reduced frequency $\frac{\omega c}{U}$, for the chord *c*, forcing frequency ω and free stream velocity *U*.

The solution of these equations can be defined using a prescribed motion of the system for a particular case of the critical flutter condition. For this case, Theodorsen defines a sinusoidal variation in the loading; therefore a solution for *h(t)* and *θ(t)* is given by the functions $h = h_o e^{jwt}$ and $\theta = \theta_o e^{jwt}$ respectively.

The Theodorsen function was an important step in understanding flutter and unsteady flow vibration in that it combined the effects of wake generation and interaction with the phenomenon of time-varying lift.

1.1.3 Flutter defined in the literature

The term flutter has been used to describe different types of aero-elastic vibration. “Flag flutter”, an unstable flapping condition of a flexible membrane with some finite stiffness subject to a flow field, is sometimes referred to as flutter in the literature [4, 5] and was offered by Theodorsen [2] as a next step in the definition of flutter where the lift and moment equations would include the dynamics due to the bending modes of the foil. Stall flutter has also been described as a process of cyclic stalling of the foil at high angles of attack [4]. In this case, the stalling is caused by the flow detachment from the downwind side of the airfoil occurring as the blade is twisted into high angles of attack due to the moment caused by the lift, or by unsteady forces on the blade. The blade then vibrates in torsion, cyclically pitching in and out of stall. The result is a flutter condition which is dominated by flow detaching and re-attaching throughout a cycle. Flutter has also been used to describe the motion of vibrating T-shaped cantilevered beams in the wind [6], a condition which does not incorporate the motion of a typical airfoil cross section, but rather, involves the motion of a non-typical t-shaped cross section normal to the wind direction. It should be noted that in Theodorsen’s description of flutter he did not place restrictions on the shape of the airfoil; he only required it to be modeled by the potential flow field [2].

1.2 Vortex Shedding

Vortex shedding and the vibration it causes are described here in order to help the reader to understand that vortex formation is an unsteady flow condition which is common to objects immersed in moving fluids, even when they are stationary. An understanding of how these vortices are formed will be extended to the mechanisms of flow that define the performance of an aeroelastic energy harvesting device.

1.2.1 Karman Vortex Street

In 1911 Theodore Von Karman [7], in studying potential flow around polished cylinders, observed the evolution of periodic vortices trailing behind cylinders in steady cross flow (figure 4). Allegedly, he got his students to polish the cylinders in efforts to eliminate the formation of the vortex street, but these efforts were, as history would show, in vain. Although the discovery is credited to Von Karman, several other researchers (Maloch [8] and Bernard [9]) are known to have touched on the subject earlier.

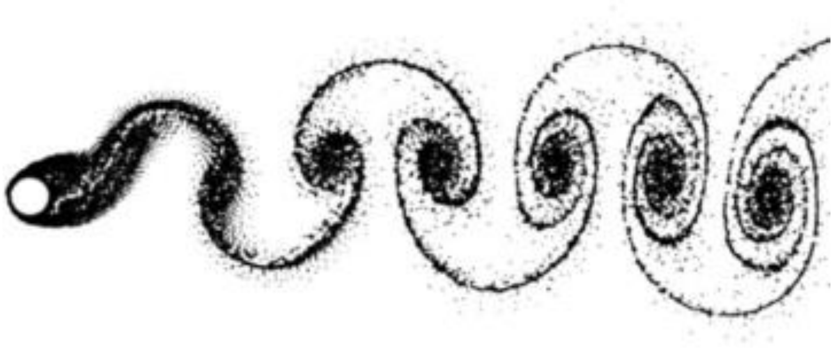

Figure 4 Top view of a cylinder in cross flow with a trailing vortex street [8]

Considering a circular cylinder in cross flow (figure 4), as the Reynolds number increases, where Reynolds number is defined as the ratio of inertial forces to viscous forces in a flow given by

$$Re = \frac{\rho U D}{\mu}, \tag{1.7}$$

where ρ is density, U is free stream velocity, D is characteristic length, and μ is viscosity, the vortex street and the boundary layer in the wake of the cylinder evolve through the changing flow regimes [1]. At low Reynolds numbers, viscosity-dominated flow, there is no vortex street observed, the wake then evolves into an alternating vortex street from $40 \leq Re \leq 3 \times 10^5$. For $3 \times 10^5 \leq Re \leq 3.5 \times 10^6$ the boundary layer over the cylinder undergoes turbulent transition where the wake structure is undefined. For $Re > 3.5 \times 10^6$ a coherent vortex street is re-established with the turbulent boundary layer over the cylinder surface [9]. Gerard 1965 [5] studied the mechanics of vortex formation and provided a useful description of the mechanisms involved by creating a qualitative description of the flow entrainment and reverse flow patterns entering the formation of a vortex in the detached wake of a bluff body. The repetition of such a system [5] leads to the alternating vortex formation seen in the vortex street.

The studies of Von Karman and Gerard investigated circular cylinders, although the vortex street phenomenon occurs in the wake of many differently shaped bluff bodies (bluff body being defined as an object which obstructs flow leading to flow separation in its wake), including flat plates normal to the flow [10,11,12], I beams, and various other types of cross sections [1]. Due to the vortex street, an oscillating pressure is generated on the surface of the bluff structure. This is a primary mechanism by which oscillating forces are induced on bluff structures immersed in a moving fluid. If the frequency of vortex shedding is close to the resonant frequency of the structure, resonance can lead to its destruction, or, in the case of energy harvesters, large amplitude motions which can be coupled to power take off mechanisms for generating electricity.

1.2.2 Strouhal number

Circa 1878 Dr. Vincenc Strouhal, experimenting with wires "singing" in the wind, characterized a dimensionless frequency value that relates free stream velocity U, Characteristic length D, and vortex shedding frequency (the "singing" pitch) f_s as

$$S_t = \frac{f_s D}{U}. \tag{1.8}$$

This Strouhal number varies with the shape of the cylinder cross section and with the Reynolds number of the fluid. Characteristic plots which show the variation of S_t with Reynolds number have been produced for different shapes [1], [13], and [14]. The relative constancy of the Strouhal number over a broad range of Reynolds numbers makes it an incredibly useful quantity in that it provides engineers and scientists with a predictive tool for determining the frequency of vortex shedding and thus knowledge about the forces which may impinge on a design or structure.

1.3 Flutter based energy harvesting research / design

This sub section introduces some previous research that has been done to understand flutter based energy harvesting and some of the relevant results and conclusions that have been described therein.

1.3.1 Non-dimensional quantities of importance

Because the power output of a vibrating power generator varies over a cycle, the parameters used to define performance are described in terms of instantaneous and averaged quantities. P_{av} is defined here as the averaged power over a number of vibrating cycles, calculated by averaging the absolute value of instantaneous power, P, measured or calculated for a given time period associated with the sample frequency. Efficiency of the device for most studies is defined as the ratio between the averaged power and the energy in the moving fluid passing through the swept area of the device at a given operating condition. Thus efficiency η is given by

$$\eta = \frac{2P_{av}}{U^3 \rho Y l}, \tag{1.8}$$

where U is the free stream velocity of the incoming flow ρ is the density of the fluid l is the length of the airfoil and Y is maximum heave wise distance traversed by the device. Y of the device is difficult to determine analytically because it changes with the heave amplitude h, the maximum angle reached by the oscillating foil θ_{max} , and the phase relationship between the two ϕ, all of which, for a self-sustained system, emerge as a result of the unsteady interaction between the flow and the device. Because of this difficulty and because of the need to have a property that is associated with the static geometry of a particular device, a coefficient of performance, C_{op}, is sometimes used which is defined identically to η with the exception that Y is replaced by the foil chord c, as

$$C_{op} = \frac{2P_{av}}{U^3 \rho c l}. \tag{1.9}$$

C_{op} is also useful in describing power output when efficiency is of less concern than the maximum power of the device. Between experiments where the foil chord remains the same, it allows performance to be analyzed while avoiding using P_{av} explicitly. C_{op} also provides a material efficiency, in that for many of these devices small size and cost of production are of large concern. C_{op} then provides a measure of performance relative to the dominant geometry of the device. It should be noted that in some studies, possibly for simplicity, η is defined the same as C_{op} [15]. Standard definitions are not yet adhered to throughout the research in this area so it is prudent to check how the value is calculated so that the conclusions are understood in context. This is a possible reason some papers quote efficiencies that go beyond the Betz limit* ([16] quotes 60% efficiency though efficiency is not calculated by the swept area rather the cross section of a d shaped pile preceding the vibrating airfoil.

Dimensionless frequency

$$f^* = \frac{cf}{U}, \tag{1.10}$$

where f is the operating frequency of the device, has shown to be a dominating factor for both flapping propulsion [17] and energy harvesting [18], where particular ratios are found to exhibit improved efficiencies over a range of chord, frequency, and flow velocities.

---

*Betz limit is a momentum-based theory for the maximum energy that can be extracted from a moving fluid, which amounts to efficiency around 59%

When Strouhal number, St, is quoted in regards to vibrating energy harvesting, it is most often the non-dimensional frequency related not to the foil chord, but rather to the wake width, that most closely follows the oscillating structure. As a rough standard it is described as

$$St = \frac{2h_o f}{U}, \tag{1.11}$$

for heaving displacement, h_o. Strictly speaking, the Strouhal number relates to the wake structure created by a bluff body in steady flow. The use of this term for an oscillating system is implying a static structural analogy to an oscillating system. Researchers, [17, 19, 20], to highlight a few, have used this value in order to include the effect of changing amplitude with changing flow conditions where the standard f^* does not take this into account. Where classical St is a function of a static bluff body creating a wake, the "*dynamic" St* relates to the wake instability and is thus used to determine a comparison between the system configuration and the wake structure it creates (this type of analysis is carried out in [18]).

The ratio of foil maximum heave displacement to foil chord,

$$\frac{h_o}{c}$$

has been shown to be useful in understanding how the heaving motion relates to the geometry of the harvester. The determination of the optimal flutter frequency is closely tied to this value where the optimal conditions for flutter energy harvesting from studies involving forced pitching and heaving include the condition that this ratio be close to or equal to 1 [18,19,21].

1.3.2 Understanding flutter energy harvesting

One of the first studies done on flow energy extraction from rigid flapping foils was done by McKinney and DeLaurier (1981) [37] where they presented their “wing mill” concept. Their investigation used experiments based on prescribed motions in heave and angular displacement to determine the feasibility of whether a ridged foil fluttering energy harvesting design “the flutter mill” could be used to generate power effectively. They concluded that the energy extraction potential was capable of rivaling that of existing rotary wind turbines. Subsequent studies have provided insight on the mechanisms affecting the performance of a device utilizing a rigid airfoil in flutter for power generation. Various aspects of the fluttering energy harvester concept have been explored. Part of the difficulty in this and any field of study is the validity of generalizing the results, which are by necessity of modeling and testing, based on particular geometries and experimental conditions. The following will give an overview of some relevant experimental work that has been done concerning fluttering energy harvesting with an effort to generalize the implications.

In a review on flutter-based energy harvesting Xiao and Zhu (2014) [33] offer 3 useful categories to describe the ways in which people seek to understand the performance of these devices.

1. Systems with forced pitching and heaving motions, FPH, where the motions of the foil, considering both heave and pitch degrees of freedom, are prescribed by the researcher.

2. Systems with forced pitching and induced heaving, FPIH, where the motion of the pitching is prescribed and the heaving displacement is a result of the aerodynamic forces on the airfoil and the elastic properties of the heave support.

3. Systems with self-sustained pitching and heaving motions, SSPH, in which both heaving and pitching are defined by the unsteady flow interactions with the elastic response of the system.

3D effects

The effect of 3-dimensional wake structures has been mostly neglected in many of the 2D numerical studies. To address this Kinsey and Dumas (2012) [31] using a 3D unsteady averaged Navier-Stokes (URANS) simulation observed the impact of 3-dimensional flow effects on an oscillating foil at a specific operating point (FPH, Re=500 000, f^*=.14, ϕ=90, θo=70^{o}). Their results showed that for airfoils of AR (aspect ratio; the ratio of the foil span over the chord, s/c) greater than 10, losses in efficiency of less than 10% should be expected when assuming a 2-dimensional approach, using endplates at the specific operating point they tested. Moreover, from the different AR tested, (10, 7, and 5), they noticed the largest drop in efficiency of 20-30 % for the AR=5 foil from the 2D predictions due to 3D hydrodynamic effects. They related this decrease in performance to an uncorrelated vortex shedding along the span (smaller peak power output when the wake does not develop evenly along the span). The study does not consider AR of less than 5, although it is clear from their analysis that AR has an effect on the ability of a specific airfoil to perform to its maximum efficiency in flutter energy harvesting, and therefore AR should be considered in performance analysis. .

Effect of the location of the rotational axis

Location of the axis of rotation, x_a, has been investigated by a number of researchers. Davids (1999) [32] used FPH based on UPOT (unsteady potential code based on a potential flow model) to show that varying the pivot location of the foil changes the optimal phase relationship between pitching and heaving. For a given pivot location there exists an optimal phase relationship corresponding to that location. In his analysis the best option (based on total efficiency) for FPH lies at the x_a of $0.3c$ (where c is chord length) [32]. For FPH this makes sense in that adjusting the rotation requires less applied torque when the axis is close to the center of pressure, approximately at the $¼c$ point [33]. Considering SSPH using a numerical approach based on a linear system model Bryant et al (2011) [34] showed the effect of pivot location on critical flutter velocity, V_c. They presented results which suggest that an optimal V_c is achieved for a pivot location just in front of the ¼ chord position for different values of torsion and heave stiffness. Moreover, they predicted that beyond $x_a = ¼c$ flutter is not possible because the “lift force now acts ahead of the hinge location, leading to static divergence of the flap rather than modal convergence” [34]. Peng and Zhu (2009) [28], investigating SSPH using numerical simulations based on a Navier-Stokes model, found that the flutter instability is sensitive to the variation of x_p and k_θ. They identified 4 different “behaviors”: no motion, regular periodic oscillations about $\theta = 0$, irregular switching between periodic oscillations about θ_o and $-\theta_o$, and periodic oscillations about some non-zero θ_o. The emerging dynamics of the system for varying k_θ and x_a are not necessarily intuitive, but a trend is seen where, for pivot locations close to the leading edge and a large enough $k_{\theta,}$ a state of no motion was observed. To induce instability in the system, a reduction in either k_θ or an increase x_a must be applied to the system. Conversely when k_θ increases the pivot point needs to be moved farther along the chord in order to trigger and maintain regular flutter. When the pivot point moves to far and the torsion stiffness is too low, irregular or sub optimal motions (which are not favorable for energy harvesting) dominate the behavior of the system.

Dynamic Stall

Dynamic stall is a process by which an airfoil experiencing a rapid change in angle of attack moves beyond its static stall angle [29]. Carr, et al (1977) [29], investigated dynamic stall for purely pitching airfoils under a variety of conditions. They described 3 distinct dynamic stall behaviors for 3 different foil types. In all cases the dynamic stall was characterized by a vortex being generated at the leading edge and then being shed along the foil, creating large normal forces and pitching moments until the vortex leaves the surface of the airfoil, at which time the moment and lift "abruptly" drop off. In their study they determined that dimensionless frequency f^* had a strong effect on the initial angle of flow reversal leading to vortex formation. At low dimensionless frequency they revealed that the vortex is often shed before the foil has a chance to reach its maximum angle of incidence, which indicates, from an energy harvesting perspective, that the correct timing of the vortex shedding with respect to the motion of the foil is imperative if one is to take full advantage of the increased lift and moment described in dynamic stall behavior. Zhu (2011) [18], in his numerical simulations looking at FPH using a Navier-Stokes algorithm, described the timing of the leading edge vortex shedding, its connection with f^* and its effect on efficiency. Consistent with Carr et al. [29] Zhu's flow visualizations show that for $f^*= 0.15$ the leading-edge vortex is well developed at the maximum angle of attack and sheds just as θ reaches 0^{o}, indicating that at the point where the “abrupt” drop off [29] takes place the foil has reached its maximum displacement in heave, a suitable point to lose lift, since heave velocity has gone to zero and with it the work being done in generating power. Zhu’s work also showed that for f^* « 0.15 the leading edge vortex is shed before the maximum displacement, leading to sub-optimal harvesting efficiency. Conversely, when f^* » 0.15, they showed that the vortex is generated too late and occurs too close to the pitching axis to generate a significant moment on the foil at the phase point where it will add the most to the work done in the system. From this we see a timing issue where, for a particular flow condition relating to f^*, there is a synchronization of the vortex shedding and the motion of the foil. The “abrupt nature” of the loss in lift on the foil indicates that non-sinusoidal motions of the pitch angle might improve performance based on maximizing the moment and lift for the point of highest angle of incidence.

Non-sinusoidal motions

Investigations of non-sinusoidal motions have been presented recently in two papers that reported the effect of FPH with sinusoidal varying heave displacement and an angular displacement which varies from a sinusoid incrementally towards a squarer wave profile. Ashraf et. al. [21], using a finite element Navier-Stokes solver model, looked at the effect of changing a pitching function so that the foil maintained a constant pitch angle for as long as possible before the switch to the opposite angle on the return stroke. They describe the changes in the function based on the change in time (fraction of the period) needed to switch angles, or as they call it, “pitch reversal time” T_r. For their trial conditions (Re = 20 000, f^* =0.127, h_o/c=1.05, and θ_o= 73°) they found that for a T_r of 0.3 they achieved an optimal efficiency that was 15% more efficient than any of the sinusoidal tests at the same conditions, and conclude that there is a favorable effect for a more square wave profile in pitching. Q. Xiao et al. (2012) [19] opted for FPH employing a numerical solution to solving the unsteady compressible Navier-Stokes equations at a low Mach number (< 0.3). A pitching function, based on a parameter β, was varied from 1 (sinusoidal motion) to 4 (where $\beta = \infty$ is a fully square wave). They found that for specific operating conditions (f^* = 0.1725, h_o/c = 1.0 and θ_o=58°) there was an optimal point, β=1.5, where there was an increase in efficiency over sinusoidal motion of as much as 50%, even over a range of St. They also showed that for $\beta = 4$ there was the greatest decrease in efficiency seen over the range of β. This indicates that while non-sinusoidal motion provides improvement, it is a subtle change that is needed.

Free play considerations, nonlinear stiffness

V. C. Sousa, et. al. (2011) [22] used numerical methods as well as experimental validation to explore the concept of combined non-linarites in the pitching stiffness of a fluttering airfoil. Their set up considered SSPH where foil pitch stiffness becomes stiffer as it reaches its maximum angular displacement (cubic hardening of the pitch stiffness). Along with the cubic hardening they introduced a region of angular displacement of the pitch degree of freedom surrounding $\theta = 0$ where zero stiffness is maintained, which they called a “free play” region. The incorporation of cubic hardening and “free play” has two effects. The free play allows the device to operate below the linear flutter speed, which means that for a given flow condition the device will be more sensitive to the initial perturbations leading to flutter, causing the V_c to drop below that which would be expected for a device with k_a acting throughout the whole displacement of θ. The cubic hardening, on the other hand, though reducing the heave amplitude at low flow velocities, improves the performance by helping to maintain reasonable heave amplitudes over a wider range of flow velocities, thus safeguarding against large displacements which could lead to damage of the device.

Power take off mechanisms

One of the major challenges in energy harvesting research is to extract electrical energy from the flow. Basically, a generator is needed that "pulls" power (damps the motion) from each cycle and converts it to electricity. For coupled-mode flutter, the kind presented here, the persistent vibration of the system is much less sensitive to damping than a single mode vibration (that may be critically damped with relatively small damping) which makes it a strong candidate for power generation [23]. For energy harvesting devices using flutter there has been a strong push towards piezoelectric power take off using piezoelectric polymers (Polyvinylidene fluoride, PVDF) due to their low cost, robustness, and increasing efficiency. Using piezoelectric, however, has shown limitations in its ability to generate electric power even marginally close to the efficiency potential predicted by experiments using prescribed damping in either numerical or experimental investigations. Low efficiency though is typical for energy harvesting devices which, because of their small size, run into losses due to aspect ratio (3D effects) and small disturbances in the flow which can affect performance.

Induction power take off has been limited in its application to flutter energy harvesting. In order to provide a benchmark for investigation, C. De Marqui and A. Erturk (2012) [24] mathematically modeled and analyzed a system for SSPH with power take off for two cases, piezoelectric coupling and electromagnetic coupling to the heave degree of freedom. For piezoelectric power take off they were able to show optimization of capacitance and resistance loads to improve power take off. For the Inductive case they found a strong dependency between internal coil resistance and aeroelastic behavior. They found the highest power output was for a load that matches the internal coil resistance, and they also determined that the flutter speed $U^* = U/\omega_h b$ (where ω_h is the heave frequency, and b is the half chord distance) decreases as load resistance increased, which effectively shows that the flutter frequency increases for increasing load resistance when U and c are held constant.

It should be noted that for any damping caused by power take off there is a risk that with too much damping the sustained flutter can be canceled out, therefore optimizing power take off must be done to consider both the efficiency of the generator and the effect that it has on the sustained motion of the device.

1.3.3 Current Energy Harvesting Devices

To date many energy harvesting devices that use aero-elastic vibration have been designed, built and tested for performance. For brevity only a select few novel devices are discussed here to provide some perspective on the current technology in terms of power expectations and scope of design.

Bryant et al. (2011) [23] designed, built, and tested their novel design which utilized a fluttering airfoil with adjustable torsion stiffness suspended downwind from a support structure via a flexible beam with piezoelectric patches at its base (fig. 5). As the device undergoes flutter, the heaving of the foil strains the beam and the attached piezoelectric patches generate current through a load. They were able to show a maximum power output of 2.2 mW at a flow velocity of 8 m/s.

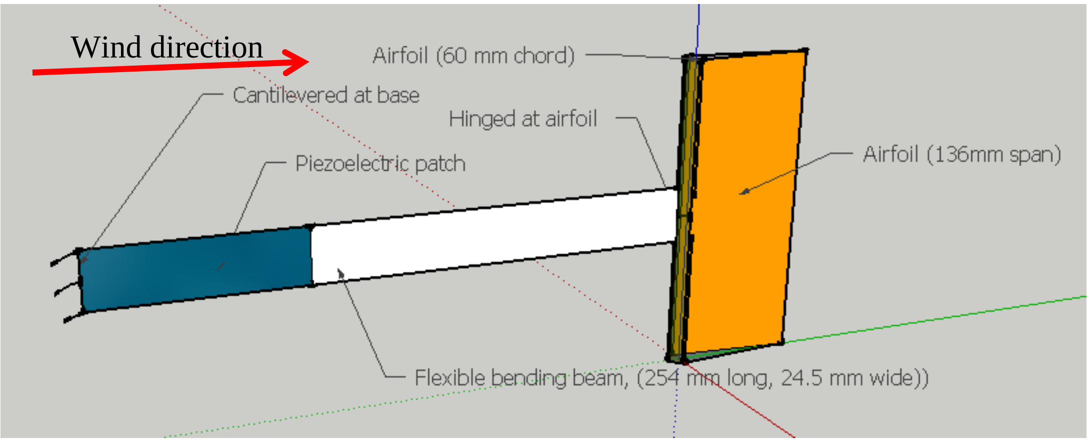

Figure 5 Novel flutter based energy harvesting device (adapted from [23])

Taylor et al. (2001) [25] developed the bio-inspired energy harvesting "eel" whereby they utilized the properties of a hyper-elastic piezoelectric PVDF (Polyvinylidene fluoride) membrane in the vortex wake of a bluff body which mimicked the motions of an eel swimming through the ocean. The bending piezoelectric membrane generates alternating voltage. With their design they proposed that due to the commercial availability of piezoelectric polymers they could provide eels cheaply to power small devices in ocean sensing equipment. The output power of the device is not quoted, although they did mention the limitations in power output due to the low piezoelectric coefficient of the PVDF membrane they were using.

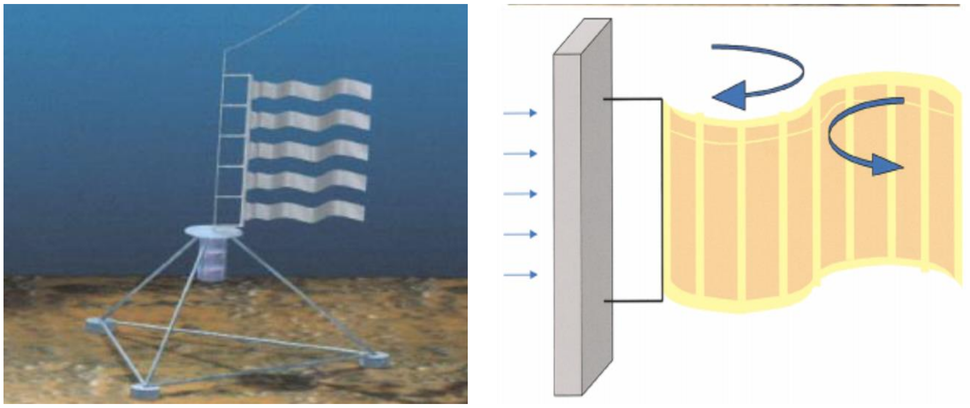

Figure 6 Energy harvesting "eel" [25]

Sirohi, J., & Mahadik, R. (2012) [26] tested a device that uses a galloping D shaped beam exciting a PZT (lead zirconium titanate) piezoelectric beam. Galloping is the vortex induced vibration of objects in cross flow (power lines, cables etc.) which is similar to vortex induced beam vibration with a twisting which imparts a varying θ over a cycle. They reported that for their particular set up (figure 6) a maximum power output of 1.14 mW was achieved. They reported that irrespective of the flow velocity or resistance (load purely resistive due to the frequency of oscillation) in the power take off circuit, the device responded at a constant frequency very close or equal to the structural natural frequency, which made it easier to tune the circuit for maximizing power output. They also noted that power output changes, depending on the natural frequency of the beam, although data revealing how much it changed were not provided in their paper.

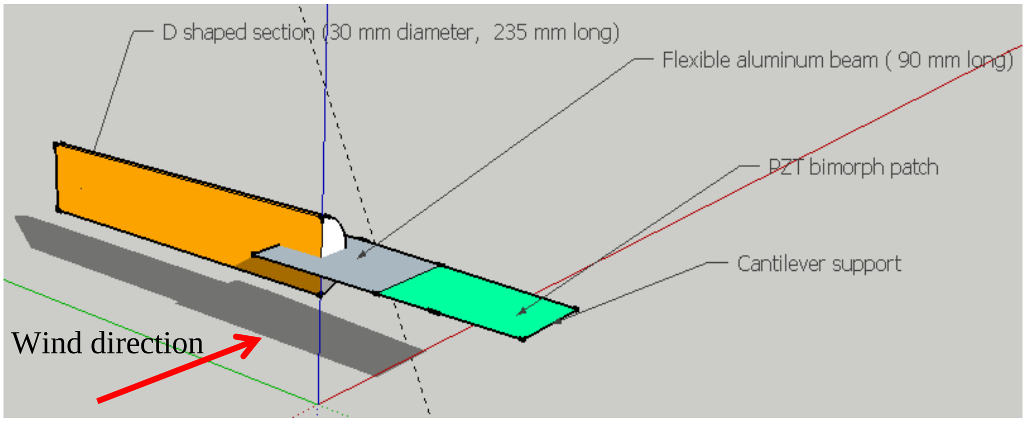

Figure 7 galloping beam harvester (adapted from [26])

The "Humdinger Wind Belt" [27] is a proprietary concept which has proven to have some commercial viability. The concept uses a belt constructed of a piece of lightweight tape suspended at both ends. As the belt is excited by the wind a flutter condition sets up on the belt and with the aid of a small magnet at one end attached to the belt, the changing magnetic field in the presence of the copper coils (mounted on either side of the magnet on the base structure) provides current to charge a battery or to power a small sensor, or both. This device has a typical cut in wind speed of around 2.7 m/s and a peak power output of ~5 mW [6].

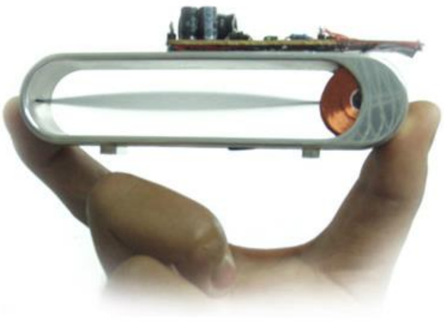

Figure 8 Humdinger wind belt harvester [27]

For their bio-inspired leaf design Li, et al (2012) [6] were able to compare the power output between two similar designs. The first used a triangular section of plastic attached on a long edge by a hinge to the end of a PVDF strip which is cantilevered behind a bluff body connection (parallel flow flutter). In the second a PVDF strip sticks up (perpendicular to the flow) with the hinged triangular section at the top of the trailing edge of the strip (cross flow flutter). They compared these two devices in power output and found an order of magnitude increase in power for the cross-flow with respect to the parallel flow one from 0.02-0.21 mW, with a maximum power for their best configuration (combination of length and amount of layers of piezoelectric material) of 0.61 mW. The designers of this device envisioned entire tree-like structures covered with these little fluttering "leaves".

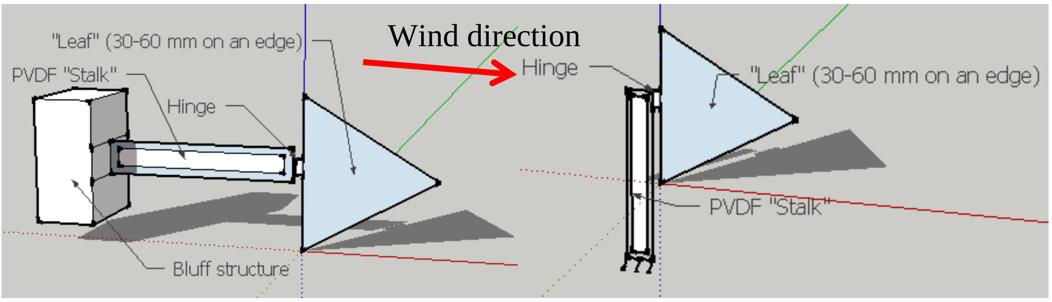

Figure 9 Two different versions of the piezo leaf generator, parallel flow left and cross flow right (adapted from [6])

1.4 Objectives and Contributions

This thesis is presenting the design and testing of a flutter based energy harvester. The goal of the investigation is to examine the performance of the harvester and to identify and quantify the variables which affect its power output and efficiency with a focus on understanding the flow dynamics which allow the flutter phenomenon to be effective in driving a generator for electrical power generation. The following report intends to describe the design process and subsequent analysis of the energy harvester. Chapter 2 provides a design overview and attempts to explain the motivations driving specific design choices. Chapter 3 and 4, the materials and methods sections, describe the tools and the experimental method used in the analysis. Chapter 5 present the results and discusses the relevance of the results with respect to how the device works (fluid mechanics and sensitivity to parameters) and the performance of the device towards the goal of improving power output and efficiency. Finally, in Chapter 5, a number of conclusions will be proposed based on the results, and a direction of inquiry will be suggested for future work, not only to improve the device performance, but also to advance the understanding of the factors which enable it to operate.

Chapter 2: Prototype Design/Instrumentation

This chapter describes the assembly of figure 10 in its components and attempts to justify the choices made for each part. Figure 10 comprises the fluttering harvester, the support structure, the base to which the upright section connects, and the wind tunnel test section that constrains the overall dimensions of the device and testing equipment.

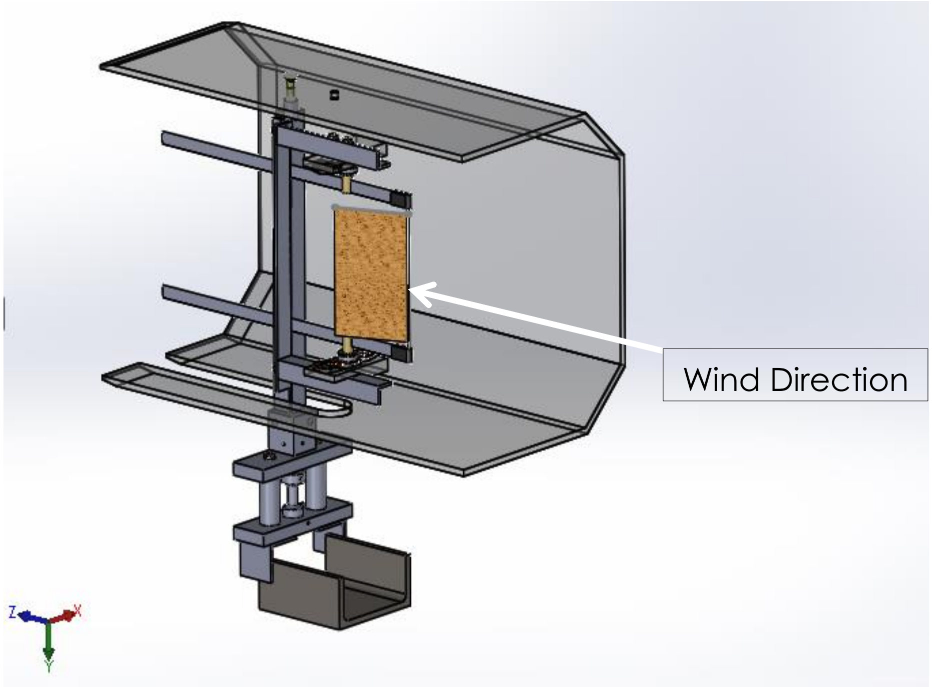

Figure 10 Harvester and base assembly

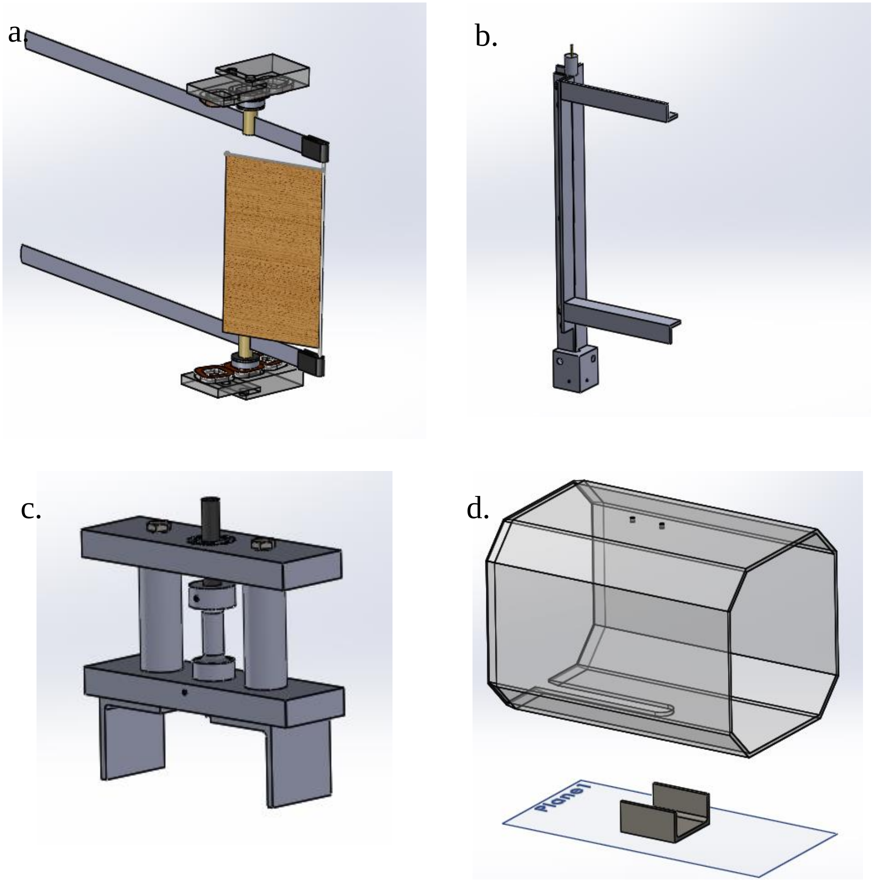

Figure 11 Components of design, a. harvester, b. upright bracket, c. base, and d. wind tunnel section

2.1 Design of harvester and experimental apparatus

2.1.1 Objectives and Criteria

Energy harvesters generally service small power requirements on the order of miliwatts to tens of miliwatts. The current design is concerned with a similar range of power potential, although there is an effort to improve the power output as much as possible, given size constraints. The current device is limited to operating within an area of 1 foot squared, the nominal dimensions of the wind tunnel cross section available for testing (Fig. 11).

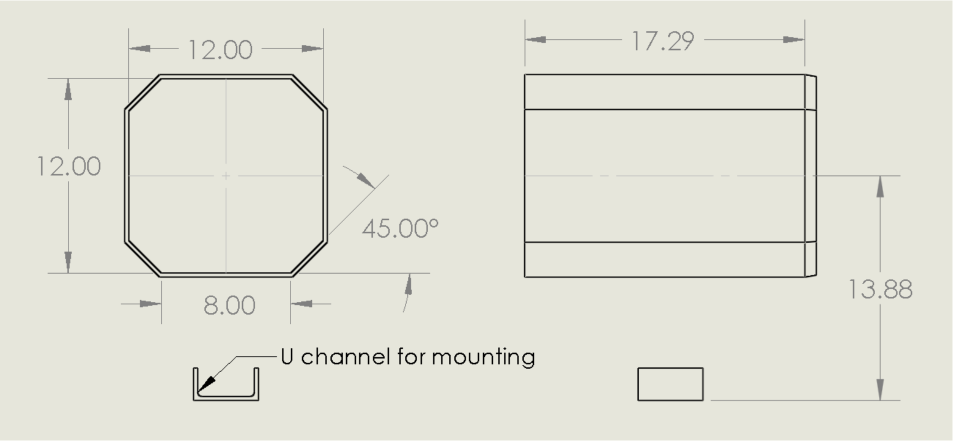

Figure 12 Clear wind tunnel test section

The harvester was designed to be simple (few parts, low cost) and robust enough to withstand heavy weather conditions. The device is intended to have a low cut in wind speed (~3 m/s) with a range that is determined through experimentation described in the results and discussion section.

2.1.2 Design Overview

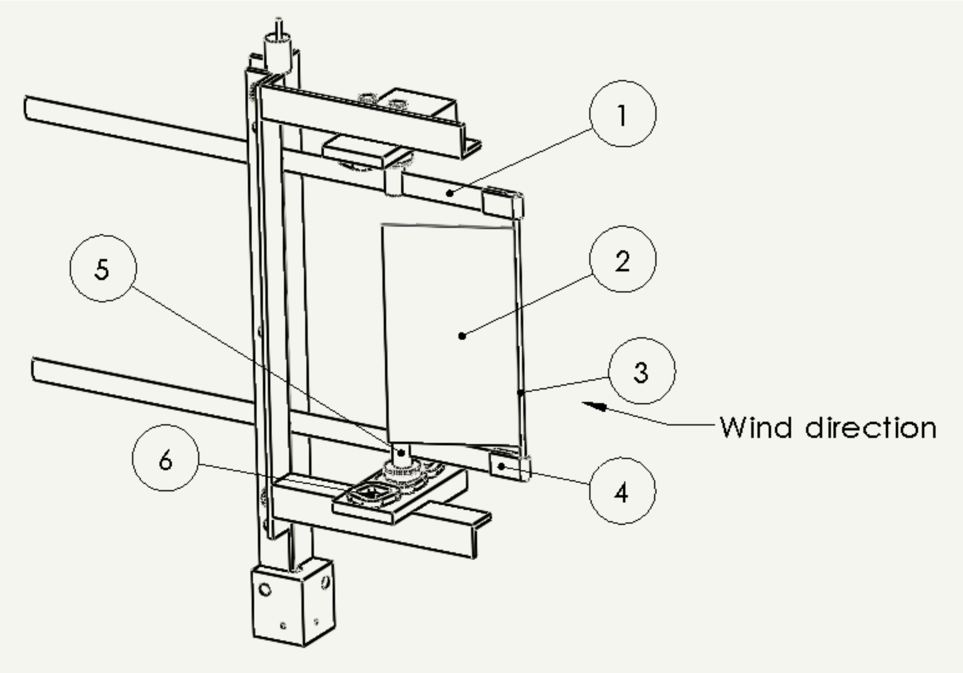

Figure 13 Fluttering device attached to upright bracket overview

The harvester is essentially a rigid, flat-plate airfoil (figure 13 item 2) free to pivot (with no stiffness) at the leading edge, with flexible beams (shown in figure 13 item 1) providing a restoring force to the heave-wise degree of freedom. The pin joint, which has zero torsional stiffness connecting leading edge of the foil to the flexible beams, in part satisfies a simplicity of design by doing away with springs coupling the foil to the support beams, moreover, it also makes it possible to investigate the performance of a flutter energy harvester device with zero torsional stiffness, which is of interest from a fluid mechanics point of view (the moment generated by the stall vortex being the only force maintaining a relative angle of attack through its motion). With regard to the pivot location at the leading edge, there is an issue regarding triggering of the flutter phenomenon; for low cut in wind speed with x_a close to the leading edge, k_θ should be relatively low [28]. Having the wind direction (shown in figure 13) uninterrupted by upstream obstacles is important for the operation of the device to ensure that the foil is subject to the free stream. Upstream obstacles (which are present in many of the devices developed to date) can attenuate the speed and disrupt the direction of flow impinging on the device which affects its performance.

2.1.3 Beam Supports

Heave-wise stiffness and heave trajectory (considering heave-wise motion as the motion which follows the bending path of the beam tip, figure 14) is controlled by the active length l and thickness t of two steel feeler gauges (figure 13 item 1). So long as the beam is clamped rigidly at its base, the cross section of the feeler gauge, being of high aspect ratio, leads to a bending motion that remains constrained in a plane. This property allows for the attachment of a magnet (fig. 13 item 5) along the span of the beam which can be used to sweep across coils (fig 13 item 6) maintaining a constant air gap between the magnet and the coil face during operation. The addition of a magnet along the length of the beam affects the mass distribution of the system which has an impact on the resonant frequency of the primary bending mode of operation given as

$$\omega = \sqrt{\frac{k}{M}} \tag{2.1}$$

where k is the linear stiffness of the beam tip and M is the equivalent mass translated to that point. This added mass also has an impact upon the momentum of the system, causing the system to react less to the dynamics of the airfoil motion and maintain a more constant frequency of operation dominated by the main bending moment of the beam, which carries the majority of the mass in the moving part of the system.

Feeler gauges are used for the beams in prototyping because their thickness can be controlled precisely, the 12 inch length provides room for adjustments, and they are readily available for purchase in many different thicknesses.

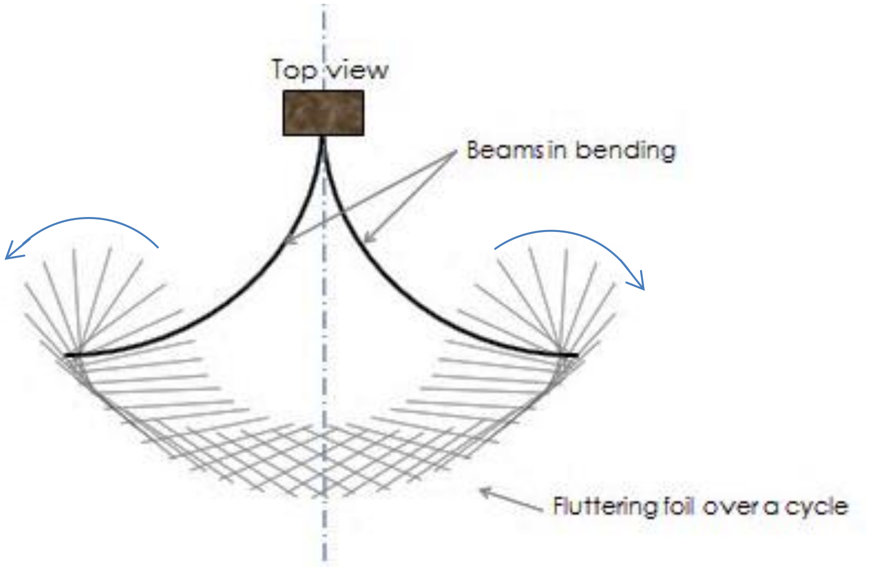

Figure 14 Top view of device in operation

2.1.4 Foil

The air foil (figure 13 item 2) is designed to be as light as possible and relatively stiff so that bending along the chord need not be considered in the analysis (or become a confounding factor). This is not to imply that a flexible foil wouldn’t improve performance; in fact, for experiments in flutter propulsion, flexibility along the chord has been considered as a way to improve operating conditions [30]. For the time being this will be left for future work to investigate. A light foil is desirable so that air moving over the foil has enough momentum to disturb its angular displacement at low wind velocities, which has been shown to be important for low velocity flutter onset [22]. The pivot location for the foil was chosen to be at the leading edge. Despite evidence from researchers suggesting that the optimal location of pivot for a fluttering harvester lies just in front of the mid-chord point for optimal efficiency [31], the pivot location for the experimental foil was chosen at the leading edge because, in the absence of torsional stiffness, the foil tended to spin on its axis during operation when the pivot was positioned behind the leading edge. A similar effect was noticed for a foil that was too heavy (too large a moment of inertia about its pivot). For the current device, the restoring force that returns the foil to its 0-degree condition is caused by the drag on the foil interacting with the free stream, which is maximized for the pivot location at the leading edge. This restoring force is overcome by the swinging foil when the foil mass is too high. The hinge attaching the foil to the axle at the leading edge is a 1/8th inch polypropylene tube along the whole span of the foil. This provides a low friction hinge as well as stiffness across the grain where the 1/16th inch thick balsa wood that is used for the foil material has the least amount of stiffness. The axle for the hinge is a 1/16th inch aluminum rod which attaches to the end of the beams via the brackets, shown in figure 13 item 4. This foil set up allows for quick exchanging of the foils between tests, a feature that speeds up testing this prototype for different sizes of foils.

2.1.5 Power take off

Electromagnetic induction was chosen as the power take-off mechanism. A piezoelectric power take off, where the piezo element is bonded to the bending beam which strains as the beam bends (bi or unimorph composite with the beam as a shim), was considered. Among the choices of piezoelectric materials, however, the charge density was found to be very low for PVDF (poly vinilidene fluoride) polymer films relative to those made of PZT (lead zirconium titanate). The PZT on the other hand is very brittle, which means that for substantial bending of the beams there is a risk that the material can crack which is a very real possibility in heavy weather conditions. Nevertheless, the potential for piezo electric power take off is possible for this particular device, as well as for piezo and inductive combinations, though again this is left for future consideration.

The design of the power take off takes advantage of the planar motion of the beam as it bends. A magnet is attached to the beam (figure 13 item 5), and as the device operates, it sweeps the magnet over coils (figure 13 item 6), which then produce a voltage across a prescribed load (circuit resistance). The coil arrangement (figure 16) was designed so that over a typical cycle, where the heave amplitude is approximately equal to the chord length, the magnet will lie within the average enclosed area of the coil array. Because of the number of variables available for adjustment, a prescribed initial estimate for the distance of the magnet x_m along the beam is chosen to be half the length of the beam for a beam length l=140 cm. This choice is not entirely arbitrary as the device has been previously adjusted, or “hand tuned”, by observation. The initial system parameters are shown in table 1.

Table 1 preliminary set up values for sizing coil assembly.

l (mm)	t (mm)	Xm (mm)	Magnet diameter (in)	Magnet thickness *(mm)*	Xm (mm)	R (Ω)	c (mm)	Foil Span (mm)	Air Gap (mm)
140	0.4	70	0.5	3.175	70	60	60	127	0.5

The coils were sized, as an initial guess, to achieve a peak voltage that would result in a peak voltage output of 6 volts for a typical operating condition of 8.5 Hz at *h/c* equal to 1.

In order to size the coils the number of turns, N, required for a circular neodymium magnet sweeping past a coil is calculated from Faraday’s law of induction

$$\frac{1}{N} = -\frac{1}{\varepsilon}\frac{d\phi_B}{dt} = -\frac{1}{\varepsilon}\frac{dBA}{dt} \tag{2.2}$$

where ϕ_B is the magnetic flux within an enclosed loop of conductor and ε is the emf (electromagnetic force) induced. In order to calculate the change in flux per unit time, the velocity of the magnet is needed at the point when its maximum cross section is moving out/in from the area bound by the conductor (the coil). A maximum velocity of 1.6 m/s at X_m along the beam was calculated as

$$V_{max} = 2\pi f d * \frac{X_m}{l}, \tag{2.3}$$

where f is the operating frequency of the device and the heave-wise displacement d represents the radius for rotation about a circle in a plane perpendicular to the plane of beam bending. The factor $\frac{X_m}{l}$ translates the velocity experienced at the end point of the beam to the position of the magnet along the length l, considering the beam as a rigid body at the point of maximum velocity. This equation is derived from the tangential velocity of a point undergoing rotation about a stationary axis

$$V_t = \omega r, \tag{2.4}$$

where ω is the angular frequency and r is the radius from the axis. The assumption (from sinusoidal motion) is that as the device is crossing the midpoint in its cycle (when the beam is straight), the velocity is purely in the heave direction, which is reasonable, considering the fact that, in general, the beam is not bending at its max velocity point . Now the field generated by a ½ inch diameter 1/8 inch thick neodymium magnet needs to be determined. Assuming a gap size of 0.5 mm between the magnet and the top of the coil and a coil thickness of 4 mm the effective gap distance is taken as 2.5 mm. This value is taken because in the region from 0.5 to 4.5mm the field strength drops off relatively linearly as obtained from the in the field strength data (figure 15) as provided from the magnet manufacturer. The magnetic field was determined through online specifications from the magnet manufacturer [35] which for a neodymium grade 40 (N40) is about 2500 Gauss at the center of the magnet to 1000 Gauss at the edge of the magnet (field normal to the surface of the magnet). Assuming a linear variation in magnitude occurs between the center and the edge of the magnet, the field, normal to the coil, is integrated across the diameter of the magnet (in SI units) as follows:

$$\int_{r}^{-r} B\,dx = 2\int_{r}^{0} (11.811x + 0.1)dx \tag{2.5}$$

The resulting field magnitude over the mid line of the magnet is found to be 0.0273 Tm. According to Faraday’s Law for an induced emf, the number of turns needed to achieve a max voltage of 6V is 137 wraps; this was increased to 140 wraps per coil for evenness. Provided the resistance in the coils is low (so power is not lost to heat), the voltage generated should theoretically create an induced magnetic field to oppose the changing one imposed upon it. Therefore, the load on the system was not considered at this point; rather, the load is to be optimized through experiment.

This analysis is not intended to provide an exact value or an entirely predictive measure of expected output, but rather, to give some justification for the set-up conditions and the size of coil that would be reasonably expected to service the intended voltage range. Because this is a highly reactive system, it was difficult to predict without a comprehensive system model how the harvester will react for a particular power take off configuration, including the one used here.

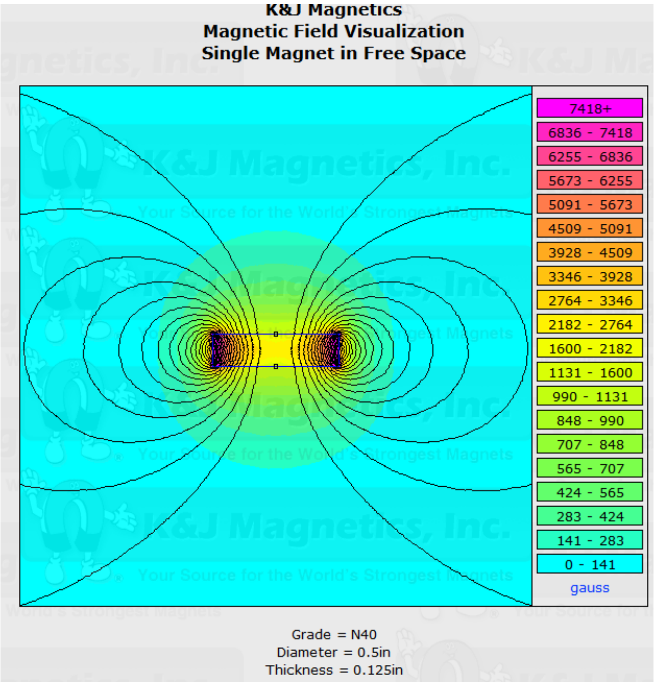

Figure 15 K & J magnetics field diagram for a 1/2" diameter 1/8" thick neodymium magnet [35]

The coil was designed so that a magnet up to 19 mm in diameter would be enclosed by the coils. This was to allow for increasing the magnet size in different trials so that the power take off could be adjusted without winding new coils. Figure 16 shows the chosen layout for coils. The coils were designed to occupy the area swept by the device operating at the conditions shown in table 1. The shape of the coils permits them to be arranged so that the midline of the coils follows the arch swept by the magnet. The coils were wired in series in such a way to allow for amplification of the voltage as it passes between two coils. The wiring diagram shown in figure 16 illustrates this effect. This configuration avoids quick polarity switches in voltage as well as maximizing the voltage generated. The result is that as the magnetic field passes over the transition between two of the coils (note: the field is only operating in a region bound by the area of the magnet), the emf generated while leaving the one coil is added to the emf produced by entering the other. Were the coils all wound the same way, the effect would be that the two sources of emf would cancel each other out.

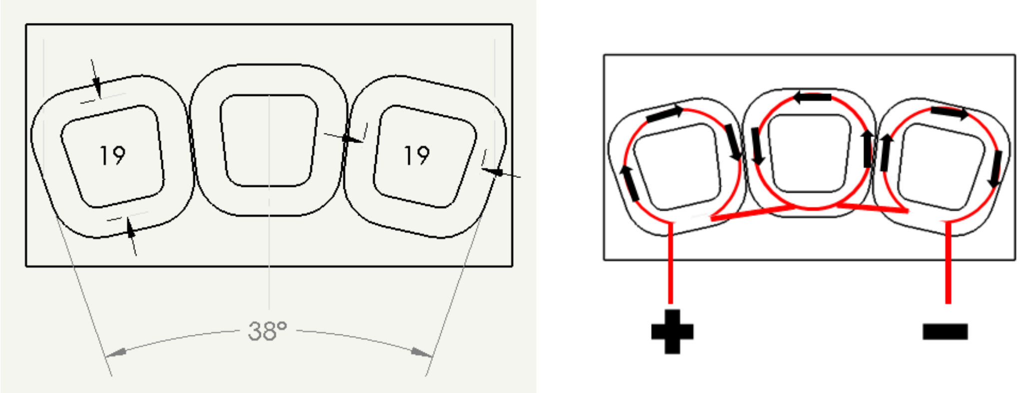

,

Figure 16 Coil layout, left, and coil winding pattern, right, dimensions in mm

2.2 Harvester Support: Design and Instrumentation

To test the harvester, a purpose-built structure was needed in order to facilitate changes in the operating parameters of beam length, the position of the coil array along the beam length, the angle of the device to the wind, and also to provide a way to measure the root moment at the base of the bending beams. The root moment is measured to provide frequency information about the operation of the device that may help to indicate what type of structures the device could be mounted on. It could also help to provide knowledge of the changing forces at the beam tip and power take off that are being translated to the root moment through the bending of the support beam, which in turn may assist with understanding the dynamic forces affecting the flutter of the device.

The specifications of the support structure are as follows:

- It must be rigid enough to avoid driving the primary bending or torsion modes with the operating frequency of the fluttering device (around 8 Hz) and constrain all 6 degrees of freedom sufficiently so as to not impede the operation of the device.
- It must fit within the area defined by the wind tunnel, figure 12.
- It should allow adjustment of the angle of the device to the wind, to permit alignment as well as observation of performance “off” the wind.
- The mounting of the power take off must permit adjustment of the coil location.
- The profile of the device must minimize blockage of the flow inside the wind tunnel.
- Beam support lengths and separation distance of the beam support positions must be adjustable.

2.2.1 Base

The base structure is both housing for the torsion sensor (figure 17 item 3) and a coupling to ground the upright section that holds the fluttering device. The structure is made of 6061-T6 aluminum, with the exception of the fittings and bearings, which are of various grades of steel. The base structure consists of two ¾” plates (figure 17 item 2) sandwiched between two ¾” columns bolted together with two ¼” 20 tpi (threads per inch) bolts (fig. 17 item 10). A torsion sensor (figure 17 item 3) is inset into the bottom plate and fixed via a set screw (figure 17, item 4). Passing through the sensor is an 8mm bolt (figure 17 item 5) which attaches to the upright section carrying the fluttering harvester.

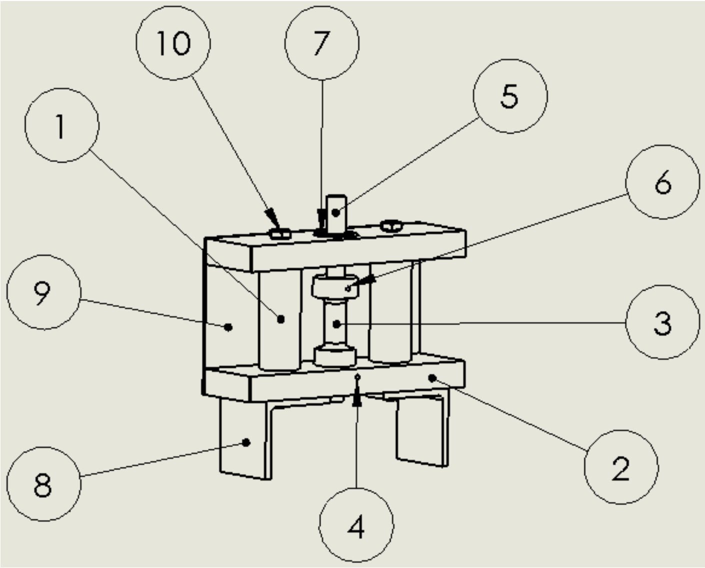

Figure 17 Base overview

The torsion imparted on the bolt by the uprights is transferred to the top of the sensor via a set screw (figure 17 item 6). The 8mm bolt is constrained at the top and bottom plate by two DGGB (deep groove ball bearing) # 608 bearings set into the outer side of both plates (figure 17 item 7). This allows only the torsional component of the forces acting on the uprights be transferred to the torsion sensor. Horizontal loads are transferred to the columns sandwiched between the two plates. In order to couple the base to the U channel, which is affixed to the table below the wind tunnel, two angle brackets (figure 17 item 8) were attached to the bottom plate via the bolts (figure 17 item 10). The angle brackets were later clamped to the U channel (located directly below the test section and fixed to the table) during operation using an 8” C clamp. A transparent acrylic cover (figure 17 item 9) was placed on both the front and the back of the base so that the wires which connect to the sensor would not be entangled or ripped off during testing.

2.2.2 Upright Bracket

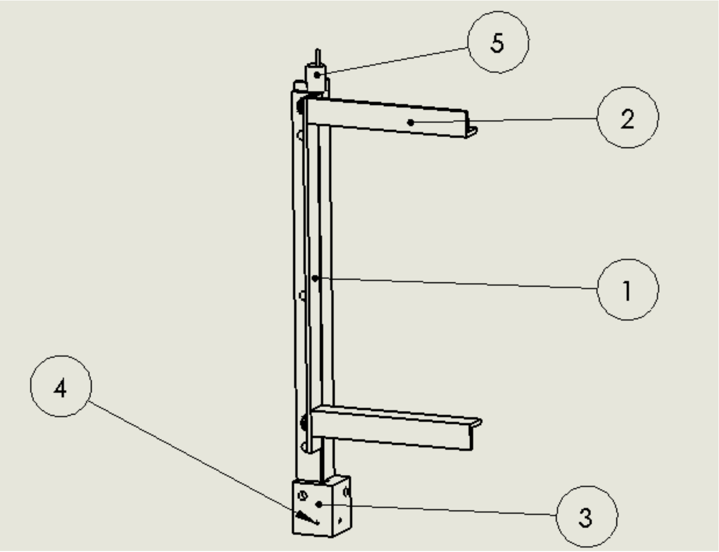

Figure 18 upright overview

The upright bracket was made from 6061-T4 aluminum with the exception of the fasteners, which are steel ¼” 20 tpi cap screws. The vertical member in the figure (figure 18 item 1) was made from 2 lengths of 3/4” (each side) aluminum angle fastened together on the inside edge. Between the two angles a piece of thin rubber was placed.

The angles thus serve as a clamp so that the beams of the harvester can be sandwiched between the two angles and clamped in place by tightening the 3 cap screws connecting the two angles. This allows for easy adjustment of the beam lengths as well as the distance they are separated from each other (allowing for different airfoil spans). The angles are fastened to the base block (figure 18 item 3) which mounts onto the 8 mm bolt in the base via a hole in its bottom, with two set screws (figure 18 item 4) in the sides of the base block rigidly fixing the 8mm bolt to the base block. The aluminum angles are connected to the base block so that the center axis of the torsion sensor lines up with the edge that constrains the beams of the harvester (figure 19).

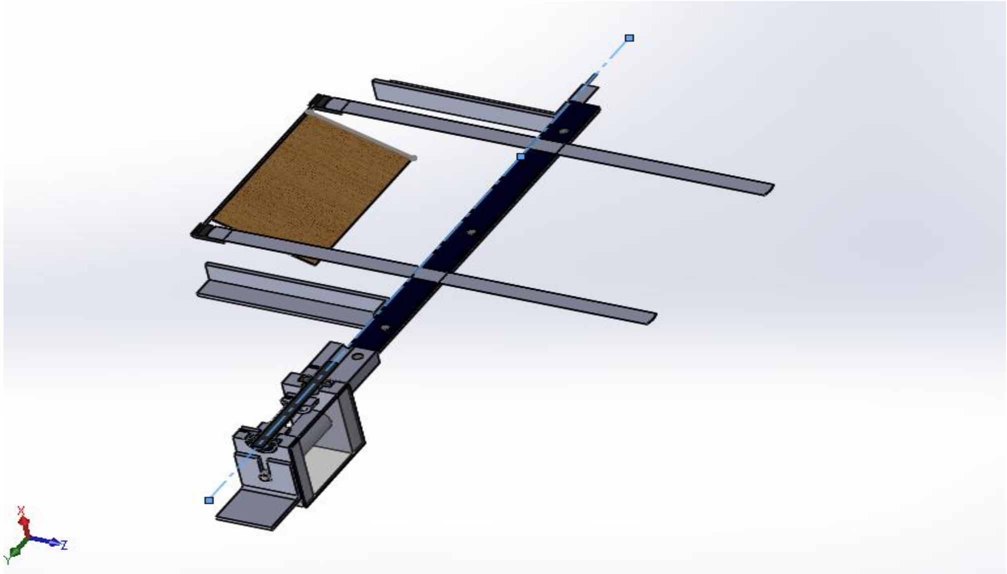

Figure 19 Cutaway showing the alignment of the beam cantilever with the sensor axis

This is to ensure that the sensor records only the moment caused by the beam bending moment, and not a combination of the beam bending moment and some shear force which would be measured as an added moment at the root were the point of cantilever not aligned properly with the rotation axis of the sensor. The two aluminum angles (figure 18 item 2) are for mounting the coils for the power take off. The fitting at the top of the uprights (figure 18 item 5), which is also aligned with the 8mm bolt, fits into a hollowed-out bronze bolt (fig 20) which is fixed to the top of the wind tunnel. This provides a hinge so that the main bending mode of the upright angles is constrained without constraining the rotational degree of freedom.

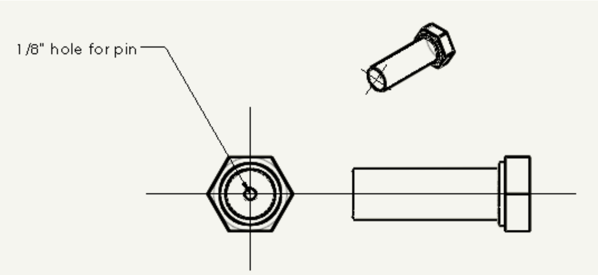

Figure 20 Bolt connecting fitting to top of wind tunnel test section

The two aluminum angles (figure 18 item 2) are mountings for the power take off coils, allowing for the coils to be adjusted along their length depending on where along the beam the power take off is required. The mountings are attached to the upright angles so that they are as far apart as possible without impacting the top and bottom of the wind tunnel. They extend at 90 degrees from the upright angles. The coil mounting structure is designed so that it can be clamped rigidly along the aluminum angle by tightening two stainless steel cap screws (fig 21). Stainless steel screws, 300 series (non-magnetic), were used here to prevent a deflecting force on the magnet as it sweeps past coils.

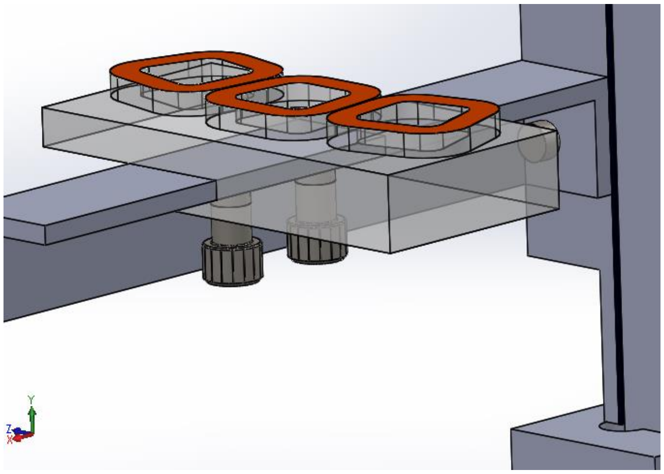

Figure 21 Coils attached to aluminum angle via two stainless steel cap screws

2.2.3 Torque Coupling Design

A torsion gauge was designed and built to measure the root moment where the beams supporting the foil are rigidly supported by the uprights. In order to accomplish this, two omega SG-4/350 rosette strain gauges were installed parallel to the z direction on the surface of the narrow section (fig 22) of the aluminum torsion coupling (figure 17 item 3). The set screws in the top of the coupling (figure 17 item 6) is used to constrain the steel shaft which carries the rotational moment of the vibrating foil. The bottom of the coupling is rigidly attached with a set screw to the grounded base. The coupling then caries the torsion through the thin-walled cylindrical section so the strain can be measured with strain gauges attached there. The two bearings in the base constrain the 3 other degrees of freedom while leaving the z translation and the z rotational moment free to be constrained by the set screw in the torsion coupling. Figure 24 shows a displacement plot of the twisted coupling for the maximum expected moment of 8 Nm.

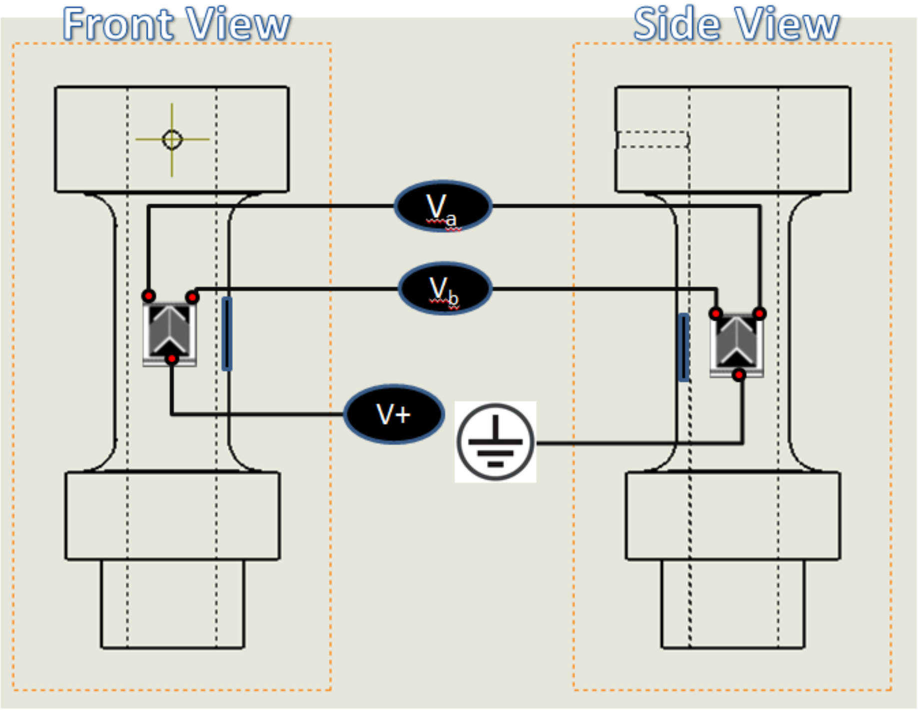

Figure 22 Sensor coupling showing strain gauges and wiring of bridge

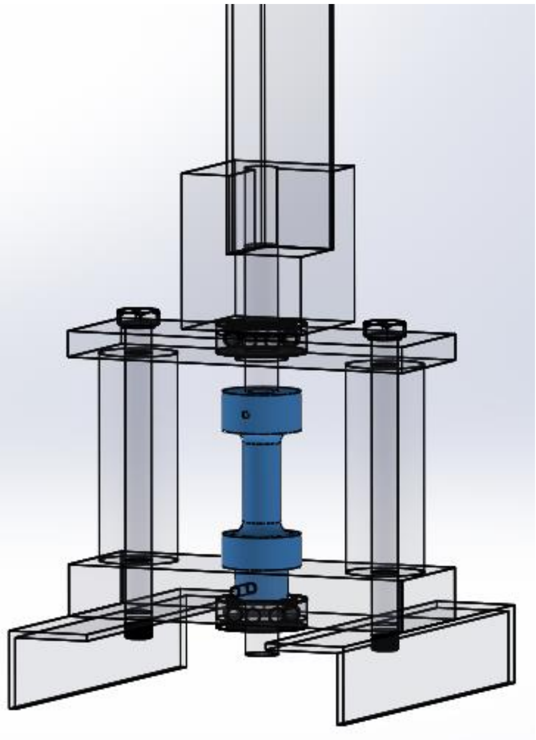

Figure 23 sensor coupling attached to base and uprights

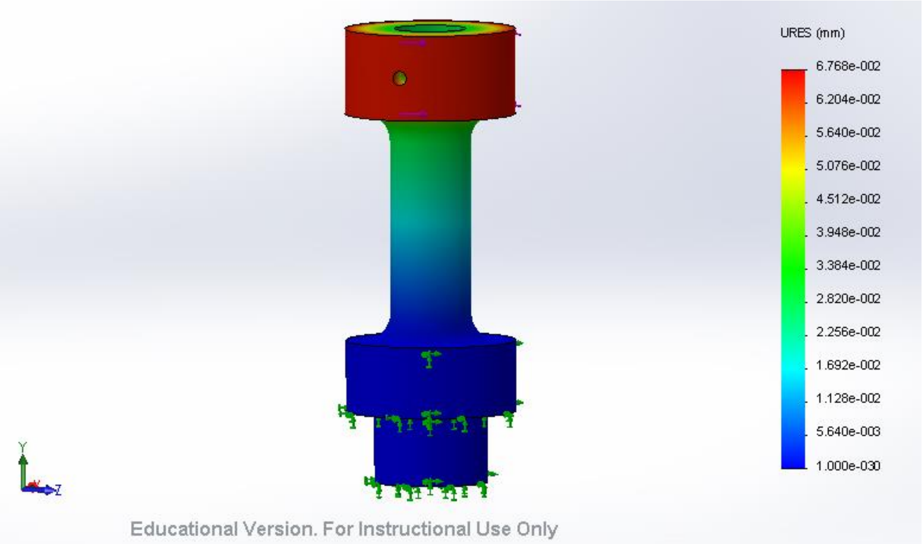

Figure 24 Displacement plot of twisted torsion coupling

2.2.4 Coupling Failure

The torsion coupling needs to allow for the greatest angular deflection over the length of the strain gauge without failure in order to maximize the signal strength. For this reason a failure analysis was done to ensure that the device would be strong enough for the assumed maximum torque.

For the maximum root moment of 8 Nm the 6061-T6 aluminum sensor coupling (material properties shown in table 2) was designed with a wall thickness to withstand the torsion to a minimum safety factor (with respect to the yield strength) of 1.5. This is quite low, but it is desirable to have the elastic strain in the thin section as large as possible, in order to get a reasonable reading in the strain gauges. The couplings’ inner bore was constrained to 8mm to fit the steel shaft which carries the rotational moment from the harvesting device. Hand calculations were compared with a FEM simulation performed in SolidWorks^{TM}. Because the design is not meant for extended use, fatigue was not considered in the analysis. Nevertheless, the design of a torsion coupling made from aluminum that is undergoing cyclical loading should consider fatigue for long-term use, aluminum having no fatigue limit.

Table 2 Aluminum 6061-T6 material properties

Material properties of Aluminum 6061-T6	
Shear modulus (GPa)	26
Elastic Modulus (GPa)	69
Poisson's ratio	0.33
Density(kg/m^3)	2700
Tensile strength (Mpa)	310
Yield strength (Mpa)	275

For the hand calculations the following formulae (taken from [36]) were used for determining the stresses in the thin, hollowed-out section of the sensor. The moment of inertia of a hollow cylinder

$$J = \frac{1}{2}\pi({r_o}^4 - {r_i}^4), \tag{2.6}$$

where *J* is the polar moment of inertia about the central axis, r_o and r_i are the outer and inner radii respectively. And the maximum shear stress at the outer wall given by

$$\tau_{max} = \frac{Tr_o}{J}, \tag{2.7}$$

where *T* is the moment applied to the section.

Considering von Misses stress criteria for ductile materials, the maximum stress, δ_{max}, for calculating yield will be $\sqrt{3}\tau_{max}$ [36]. For the safety factor of 1.5 the wall thickness was found to be 0.684 mm. For ease of machining and conservativeness this value was increased to 0.75mm to produce an inner diameter of 8mm and an outer diameter of 9.5mm. A SolidWorks^{TM} static loading simulation was used to validate this calculation to observe any unforeseen stress concentrations due to the particular geometry of the sensor design.

Using Solidworks^{TM} simulation package for static stress analysis, the working boundary conditions were applied to the coupling and a moment of 8 Nm was imposed. A test of the FEM solution was performed using successively smaller element sizes in order to confirm convergence of the FEM solution. Figure 25 shows the relative error, calculated as the difference between the current and last maximum stress solution, as a function of mesh parameter.

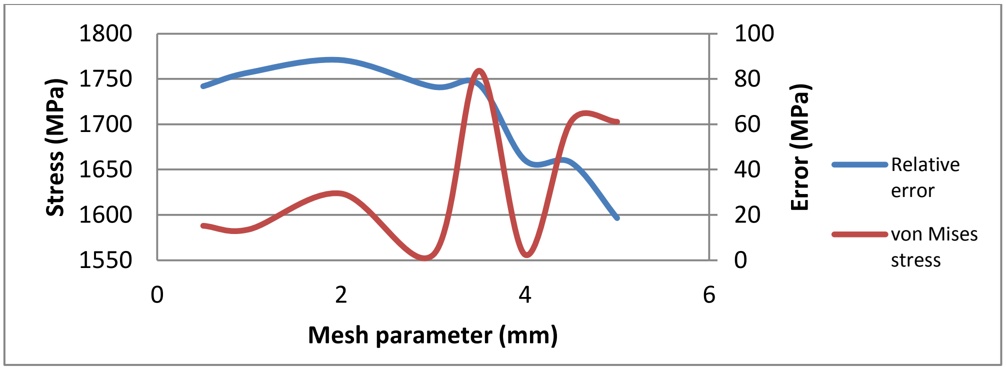

Figure 25 Solution convergence of FEM simulation

The final maximum stress value of 174.19 Mpa located at the thinned out section in the sensor at a converging relative error of 1.5 MPa was found leading to a safety factor of 1.58 which helps to confirm that the 0.75mm wall thickness was a conservative choice.

2.2.5 Coupling Strain Gauge Performance and Amplifier Specifications

In order to specify the amplification for the strain gauges used on the thin wall section the maximum expected change in resistance is calculated from the GF (gauge factor) of the strain gauge (provided as 2.0 which is the relative change in resistance over the strain) uncertainties not considered here, since the purpose of this analysis is only to provide an operating range. The formula for the shear strain in the thin wall cylindrical section in radians is given by

$$\gamma = \frac{\tau}{G}, \tag{2.8}$$

where G is the shear modulus of the material and τ is again the shear stress at that section. From τ_{max} provided by hand calculations at the 0.75 mm wall thickness (95.6 MPa), γ_{max} is calculated to be .0036 radians or 0.2 degrees.

In order to provide a measure of strain, the strain gauge is oriented at 45 degrees to the axis of torsion so that the angular displacement of the hollow section leads to a change in length of the foil in the strain gauge (figure 26 shows the conformational change due to shear strain τ). For the calculation of the change in resistance in the gauge, the surface of the tubular section is considered flat. As shown in figure 26, the change in length of the 3.8 mm foil section due to a shear displacement is given by

$$\delta = \frac{\sin(45) * L}{\sin(45 - \gamma)} - L, \tag{2.9}$$

which yields a strain of $3.5*10^{-3}$ or 3500 μ. From the gauge factor this corresponds to a change in resistance given by

$$\Delta R = R * GF * Strain, \tag{2.10}$$

with each strain gauge section having a resistance, R, of 350 Ω, the ΔR due to the strain caused by the 8Nm torque is 2.59 Ω.

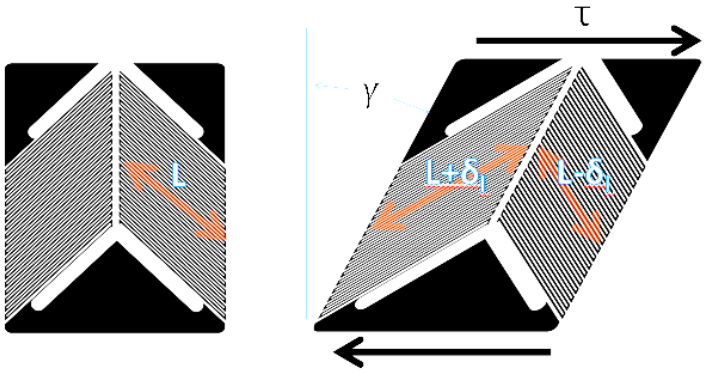

Figure 26 Strain gauge unstrained and strained showing variables of interest

A full bridge circuit was used to wire the strain gauges shown in figure 27. This configuration allows for the amplification of voltage change due to changes in resistance from contraction and extension of the sensor foil material. A source voltage for the bridge and the amplification circuit is provided by the 5V source in the DAQ (digital acquisition device). From this 5 volt source (V_i) an amplification of the output voltage from the bridge is desired to give a 5-volt signal peak-to-peak for the maximum strain expected in the sensor. From the change in resistance in the 4 strain gauges, the V_o (output voltage V_a-V_b) from the bridge is given by

$$V_0 = \frac{V_i \Delta R}{R} \tag{2.11}$$

From this the output voltage is calculated as 0.037V. The assembly therefore requires an amplification of approximately 67.57 times for the maximum expected moment to reach 5 volts peak-to-peak.

A LMC6482 operational amplifier was used in the circuit shown in figure 28 and it was tuned with resistors to get close to the prescribed amplification. The values of R_1 and R_2 in figure 28 were chosen to be 1kΩ and 1MΩ respectively, leading to an amplification of 100 times according to

$$Gain = \frac{V_{output}}{(V_a - V_b)} = \frac{R_2}{R_1}. \tag{2.12}$$

Although the resulting gain is more than prescribed, it was decided that slightly more sensitivity would be prudent, since the working range of the sensor likely will be far below the maximum expected strain. With these parameters the torque coupling varies its voltage depending on the level of torque on the support due to the forces imparted on it by the vibrating energy harvester. The voltage will be compared in experimentation with known torque values and calibrated over a range that compares with the expected range of input torque to be experienced during operation.

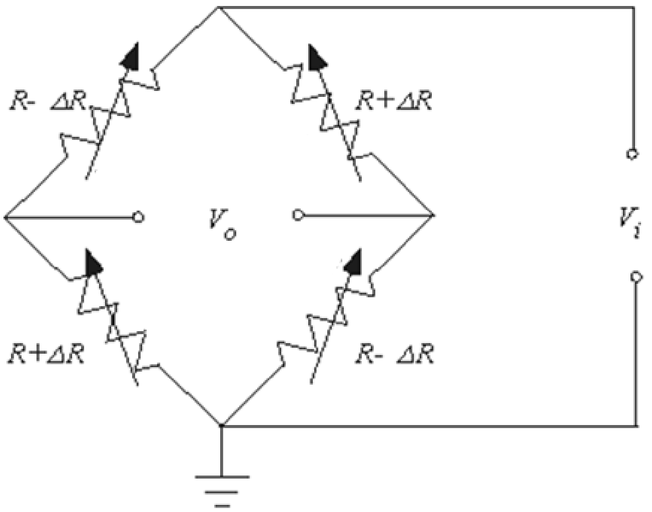

Figure 27 Full bridge circuit

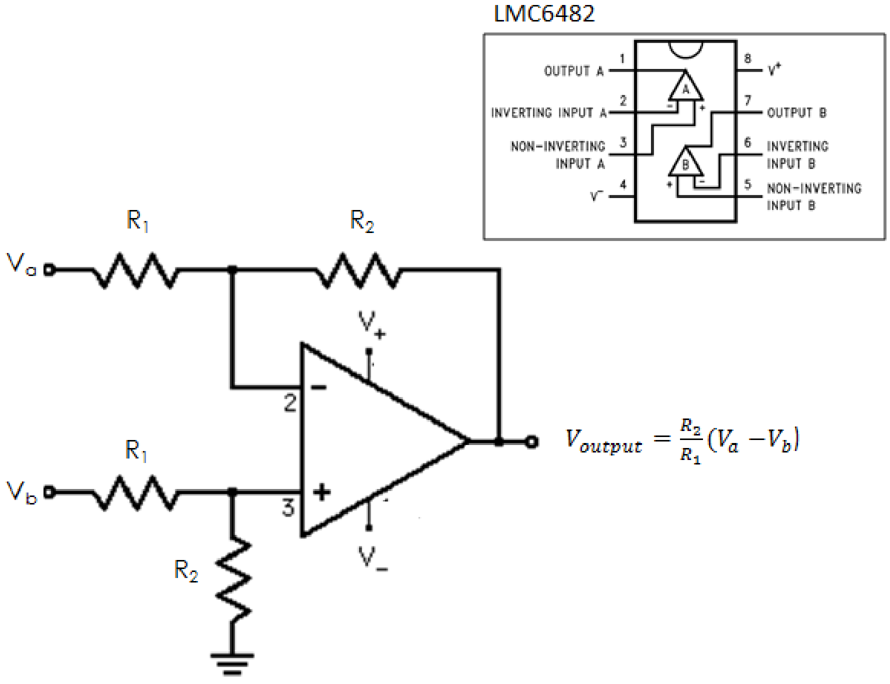

Figure 28 Amplification circuit

Chapter 3: Materials

3.1 Wind Tunnel Apparatus

The wind tunnel is made up of three sections. The section to the left of figure 29 is the low speed inlet, which aligns parallel flow by way of a honeycomb tube array in the flow direction. The section in the center of the wind tunnel is the test section and is made of clear Plexiglas for viewing experiments. Both the test section and the inlet slide to the left inside guides bolted to the Formica tabletop, as shown in figure 29, to allow access to the equipment being tested. The wind outlet section has a 3-blade fan, powered by a 1.5 kW motor at its outlet, which pulls air through the tunnel. The wind speed is regulated through a control knob, which varies the power supplied to the motor. The overall dimensions of the machine are 2.98 m long, 1.83m high, and 0.8 m in width. The area of the test section is 300 mm x 300 mm with a length of 450mm. Both the inlet and outlet sections are fabricated with a thick fiberglass shell and both are bolted rigidly to the tabletop to avoid shaking of the structure during operation.

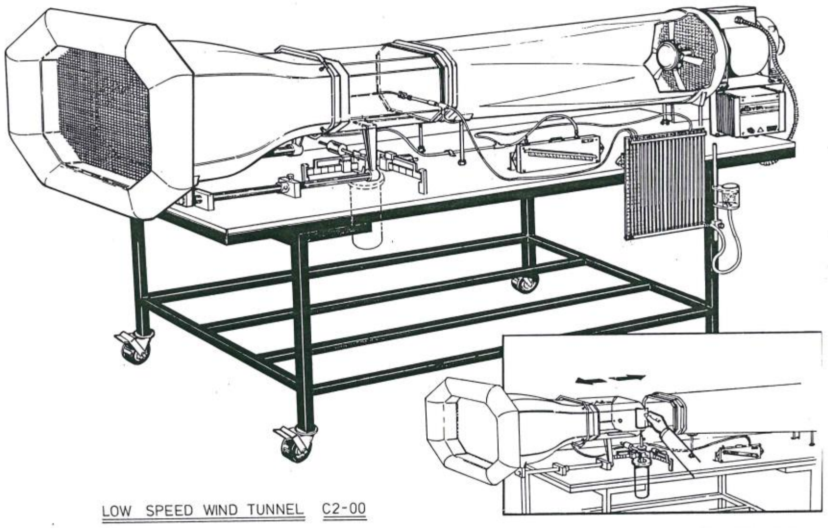

Figure 29 Wind tunnel

3.2 Wind speed measurement

Wind speed is measured using a Kestrel 1000 Wind meter, figure 30. The measurement precision is rated to ±3% of reading. Measurements were taken with the flutter device operating at steady state with the wind meter mounted mid channel along the center line of the test section. The wind speed measurement was taken 30 cm upstream of the operating device, inside the constant cross section of the test section; consequently, unsteady effects due to the wake of the installed apparatus were assumed not to interfere with accurate wind speed measurement.

Figure 30 Kestrel 100 wind meter

3.3 Imaging

High-speed imagery was recorded using a Casio EX-ZR200 digital camera. The images were taken at 420 frames per second at a resolution of 224 by 160 pixels. The camera was mounted 60 cm above the top of the test section and held in place by a purpose-built camera mount clamped to the table top. The camera's lens was zoomed in to include in its frame the width of the test section. The camera was mounted as far away from the operating device as possible so that effects due to perspective would be minimized. The data for experiments was all taken from the same focal plane in the images being the plane traced by the top edge of the airfoil.

3.4 Voltage Measurement

Amplified voltage across the sensor bridge and the voltage across the load on the power take off were recorded using a National Instruments NI-USB 6008 DAQ (digital acquisition device) at a sample frequency of 500 Hz. The DAQ (figure 31) was interfaced with Lab View software to save and convert the data of each experiment to a Microsoft Excel file for post-processing. Figure 31 shows the DAQ and figure 32 shows a screen shot of the VI (virtual instrument) produced using Lab View to collect, display and export voltage data. Two outputs on the VI represent the Load and the Sensor voltage, while the third is the calculated instantaneous power, according to

$$P = \frac{{V_R}^2}{R} \tag{3.1}$$

where V_R is the voltage across the load and R is the resistance of the load. Allowing Lab View to calculate the instantaneous power expedites the post-processing in MS Excel.

Figure 31 National instruments NI USB-6008 DAQ

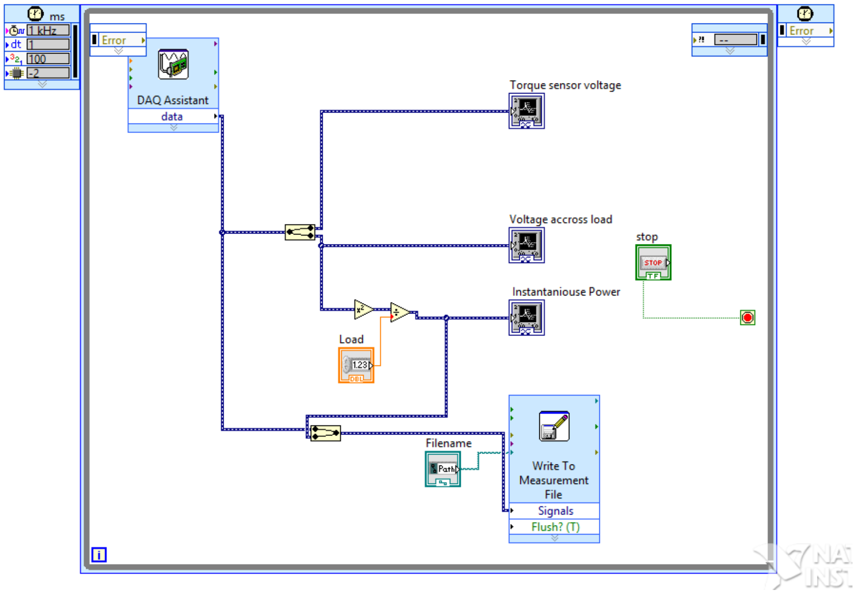

Figure 32 Lab View virtual instrument for measuring voltage

3.5 Mass Measurement

Mass measurement for the calibration of the torque sensor was conducted using a Jennings JS-50X pocket scale. Due to the unavailability of a data sheet, the error in the measurement was assumed to be half of the minimum significant figure $\pm 0.05g$. This accounts for the maximum error incurred in rounding, and could also be described as a quantization error for this digital scale.

3.6 Post-Processing

Post-processing of voltage measurement data was done using Microsoft Excel. Statistics functions, including calculation of variance, standard deviation, mean, kurtosis, and skew were used for analysing data based on multiple, replicated measurements. The FFT (fast Fourier transform) was used to calculate dominant operating frequencies from strain gauge measurements. MS Excel provided the series of harmonics for the data set of 4096 samples at sample frequency (f_s) of 500 samples per second, leading to a frequency bin size (minimum frequency resolution) of

$$\frac{f_s}{4096} = 0.122\ Hz$$

Thus the error in the frequency measurement was taken as half of this bin size$\pm .061\ Hz$. The frequency error was assumed to be uncorrelated to the error associated with the measurement of the torque, due to the inherit averaging that takes place for the large sample size. The frequencies of interest, at least for the measurement of the vibration of the operating device, were on the order of 10 Hz; thus, for the sample size, the frequency determination was averaged over approximately 82 cycles. For this reason, the error in the frequency was assumed to be dominated by the minimum resolution in the FFT rather than the quantization and noise in the voltage measurement.

Error associated with the voltage measurement was defined by the quantization error in the measurement~~;~~ the minimum step in the digital representation of the analogue signal. In this case the quantization error in the voltage reading was $\pm 0.0025V$. Error associated with noise was determined by calculating the maximum voltage reading with no load on the system:$\pm 0.012V$. Combining these errors leads to an overall error associated with voltage acquisition of $\pm 0.0145V$.

Post-processing of image data was done using Image J software, which allows the scaling and measurement (angle and distance) of imported images. Measurements of θ and h for the operating device were taken to describe the motion of the device over a cycle. Images were also constructed using Image J to depict the motion of the device over a cycle. Image J is an open source program designed to provide a free tool for researchers and scientists to conduct various types of operations on image data. Image J was downloaded from http://imagej.nih.gov/ij/. Errors associated with distance measurements were estimated from the pixel size of the images being measured and from the uncertainty in position due to the frame rate. Pixel size after image scaling was measured as less than 1 mm, since the measurement of h was performed only when the bending beam was at zero velocity, a relatively small uncertainty with respect to the fast moving foil was recorded. Maximum angle θ was measured close to the maximum velocity position, although its value remains relatively constant over several frames due to the low angular velocity at maximum θ. Therefore, errors due to frame rate are approximated to be on the order of error due to resolution, leading to an assumed uncertainty of h measurement of $\pm 1mm$. Uncertainty in angular measurement of the angular diversion that would be caused by an error of 1mm on the maximum foil size was calculated as follows:

$$\sin^{-1}\left(\frac{1}{80}\right) = 0.716{\sim}\ \pm 1\, degrees$$

Chapter 4: Methods

4.1 Experimental Design

4.1.1 Torque Sensor Calibration

The torque sensor was calibrated by applying a known force 0.284 m from the rotational axis along a beam rigidly attached to the sensor shaft (figure 33). The applied force was measured by clamping the base to the table and measuring the force between a scale and the cantilever beam as generated by slowly unscrewing a nut and bolt to create a force between the beam and the scale. The formula for torque of a force applied about an axis of rotation is

$$\tau = mgr, \tag{4.1}$$

where m is the measurement of mass in the electronic scale used in the experiment, g is the acceleration of gravity, and r is the distance from the rotational axis. Torque measurements were recorded along with corresponding force measurements. The data were then used to create a calibration curve for the torque sensor. This calibration curve was used to determine torque values from voltage data collected from the sensor.

Figure 33 Set up for torque measurement

4.1.2 Load Optimization

In order to determine the optimal resistive load for the harvester during operation, the harvester power is measured for different values of resistive load running at specific set-up and flow conditions (table 3). A purely resistive rather than reactive load is used due to the relatively low frequency of operation, around 8-9 Hz. A more detailed optimization considering reactive loading could be done though for now the literature available on load optimization for fluttering harvesters only considers resistive loading on a inductive system [24]. The load is controlled via a potentiometer which varies the load between 0.167 and 8.33 times the resistance of the coil array, the coil array having a resistance of 60Ω (defined by 6 X 10Ω coils wired in series). Based on experiments using numerical analysis for flutter based energy harvesting [24], it was assumed that the optimal load would correspond to a load, R, which matches the system resistance, R_s. Therefore, a higher density of measurements and repeat trials were prescribed for the area surrounding the system to a load ratio (R/R_s) of 1, in order to define more precisely the expected inflection point and to provide a measure of random error in the region of interest. If maximum power were to fall outside of the expected range, the experiment could be repeated for a different range of load values. Table 3 indicates the system set up for the optimal load characterization and Table 4 to shows the specific resistive values used.

Table 3 System set up for determining optimal load on the system

l (mm)	t (mm)	Gap (mm)	Magnet (diameter in)	Xm (mm)	R (Ω)	c (mm)	U (m/s)
140	0.4	0.5	0.5	70	varied	60	4.1152

Table 4 Experimental treatment for optimal resistance

R (Ω)	500	300	200	170	150	140	120	110	100	90	80	70	60	50	40	30	20
# of Trials	1	1	1	3	3	3	3	3	3	3	3	3	3	3	3	3	1

4.1.3 Harvester Performance Investigation

The performance of the harvester can be considered in many ways. For clarity, the investigation is considering performance of the device with regard to average power output and efficiency. An empirical analysis of the fluid dynamics comparing the high-speed video of the device in operation (providing information about changing θ and h) to the torque was also carried out. The fluid structure interactions were correlated to the performance variables of the system in an effort to better understand how the dynamics of this particular system relate to performance. Due to the large amount of adjustability in the system, and considering the number of variables shown in table 5 (all adjustable), fully observing the performance of the device under every conceivable combination is beyond the time limitations of this study. In order to constrain the investigation to a manageable amount of experiments, a choice was made to consider the performance with respect to the changes in foil chord (all other variables remaining constant) with the treatment of changing wind speed. This choice provides a way to observe the effect of changing f*. Table 5 provides shows the set up parameters used for the first experiment for varying chord and Table 6 shows the chord and wind speed values to be used along with the corresponding and f^* values at the assumed vibration frequency of 8.5 Hz (this frequency value is gathered from preliminary tests) .

Table 5 System set up for investigating device performance over range of chord values

l (mm)	t (mm)	Gap (mm)	Magnet diameter (in)	Xm (mm)	R (Ω)	c (mm)
140	0.4	0.5	0.5	70	60	Varied

Table 6 l Treatment for changing chord and wind speed, *f values for 8.5 Hz**

	Wind Speed (m/s)				
c (mm)	3	3.5	4	4.5	5
40	0.113333	0.097143	0.085	0.075556	0.068
50	0.141667	0.121429	0.10625	0.094444	0.085
60	0.17	0.145714	0.1275	0.113333	0.102
70	0.198333	0.17	0.14875	0.132222	0.119
80	0.226667	0.194286	0.17	0.151111	0.136

The values of chord used in the experiment were chosen considering the physical limits of the device. Beyond a chord of 80 mm the device begins to have difficulty operating under most wind speeds. In addition, below 40 mm the motion during operation begins to diminish (from observation) over most average wind speeds. The combinations of chord and wind speed have been chosen to provide a range of f^* which includes an f^* of 0.15, which has been quoted as an optimal point for performance of harvesters of this kind [18]. The investigation not only seeks to confirm this finding through a physical experiment, but also aims to determine what chord size will provide the highest power output for this particular device. Because h_o/c and θ also have been shown to be a consideration for optimal η, a range of f^* values were chosen for different foil sizes with some overlap, in hopes that a range of h_o/c and maximum θ would emerge from the experiments. If it can be shown that for SSPH-a maximum efficiency is found for θ and h_o/c of ~90^0 and ~1 respectively at an f^* of ~0.15 then this study would be the first experiment (from the references gathered) to confirm this as an optimal case for SSPH. Moreover, the ability of a system working in SSPH to drive itself to this optimal condition merits discussion.

Using the experimental matrix of Table 6, each experiment was repeated 3 times in order to evaluate experimental error. The assumption was that the experimental error between tests can be modeled as a normal distribution that can be used to quantify the experimental error as a standard deviation from the mean.

For each trial the device is allowed (given time) to reach its operating amplitude before measurements are taken. Data for the voltage across the load R and the amplified voltage change across the strain gauge bridge V_o were recorded via the Lab View virtual instrument at a frequency of 500 Hz for 5 seconds (The device was given time to settle into an operating state with no observable transient behavior between cycles). For the same operating conditions, high speed video imagery (420 fps) of the device operation was recorded so that the angle of the foil to the wind (θ) and the heave displacement (h_o) could be monitored as they changed throughout the motion of an oscillating cycle.

4.2 Uncertainty and Sources of Error

For repeated experiments the random error will be approximated in terms of standard deviation from the mean, $\sigma_{\bar{x}}$, which is calculated from the standard deviation, σ_x, as

$$\sigma_{\bar{x}} = \frac{\sigma_x}{\sqrt{N}}, \tag{4.2}$$

where N is the number of repeats in the experiment and

$$\sigma_x = \left(\frac{1}{N}\sum_{i=1}^{N}(x_i - \bar{x})^2\right)^{1/2}, \tag{4.3}$$

and

$$\bar{x} = \frac{1}{N}\sum_{i=1}^{N} x_i. \tag{4.4}$$

When observations were recorded from a device or scale, an assumed error value was taken in accordance with the precision of the measurement device. In general, one half of the highest precision of the device was accepted as the error. For example, for a scale with divisions up to 1mm, an absolute uncertainty of 0.5 mm would be assumed for all measurements made with that device. With respect to quantization of error of analogue-to-digital conversion of voltage data, the error was recorded as half the magnitude of the quantization step in the recorded voltage scale, as well as an added error to account for noise in the system.

Propagation of errors when calculating quantities--such as η and f^*, for example--which are comprised of several variables with various errors associated with each, is done with respect to the variance formula for error propagation

$$\Delta f\left(x_1, x_{2,} x_3 \ldots\right) = \sqrt{\left(\left(\frac{\partial f}{\partial x_1}\right)^2 \Delta {x_1}^2 + \left(\frac{\partial f}{x_2}\right)^2 \Delta {x_2}^2 + \left(\frac{\partial f}{x_3}\right)^2 \Delta {x_3}^2 \ldots\right)} \tag{4.5}$$

where f is some function of any number of independent variables, and assuming continuous differentiability of the function f with respect to its constituent variables. For the current investigation, it was assumed that variables and sources of error are independent and correlation is minimal or negligible.

4.2.1 Strain Gauge Calibration

The identified sources of error in the measurement of the strain gauge torque are as follows:

1. Measurement error of electronic scale $\pm 0.05g$
2. Error of voltage measurement from the sensor bridge $\pm 0.00145V$
3. Random error between experiments due to unknowns

The error due to the first two is quantifiable, but the third needs to be calculated from the resultant calibration curve and the deviation of the measured points from that curve. The calibration of the strain gauge is assumed to be linear due to the documented behavior of the strain gauge. Therefore, a random error was calculated from the standard deviation of the difference between the measured values and the calibration line. In order to ensure a normal distribution of the deviation of the points from the best fit line, skew and kurtosis (derived using statistics tool in excel) will be used to help to verify (due to the large number of points) that the variation from the best fit line is close to a normal distribution.

4.2.2 Optimal Resistance

The identified sources of error in load and power measurement are as follows:

1. Measurement error of the load due to uncertainty in the resistance measurement, $\pm 0.05\Omega$
2. Quantization error of voltage measurement across the load, analogue to digital conversion, $\pm 0.0025V$
3. Measurement error due to uncertainties in the wind measurement, $\pm 0.025\ m/s$
4. Random error in between experiments due to unknowns

The error due to the 4th source was dealt with through experimental replications. The experiments that fell close to the inflection point for optimal power were repeated 3 times in order to provide a measure of the uncertainty using $\sigma_{\bar{x}}$.

4.2.3 Harvester Performance Evaluation

The identified sources of error in quantities measured for the evaluation of performance are:

1. Quantization error of voltage measurement across the load and sensor bridge analogue to digital conversion $\pm 0.005V$
2. Measurement error of set up parameters due to precision limitations of ruler used during set up $\pm$ 0.5 mm
3. Error in measurements of high-speed video due to low image resolution $\pm$ 1 mm (relates to error in angle measurement)

4. Random error in between experiments due to unknowns

The error due to the 4rd source is dealt with by experimental repeats. All experiments are repeated 3 times in order to calculate a measure of the uncertainty using $\sigma_{\bar{x}}$. Errors due to small amounts of noise, on the order of 0.01V are not considered because averaged quantities are calculated over 10s of cycles, which, assuming the noise values observed are normally distributed about the average value, tends towards the average as the sample population increases. Therefore the random error calculated from experimental repeats is considered to dominate the uncertainty in those quantities, namely averaged torque and power.

Chapter 5: Results and Discussion

5.1 Torque Sensor Calibration

Thirteen voltage measurements were recorded while increasing a known force applied to the end of the lever arm attached to the base block, and ten measurements were recorded as the known force was decreased to zero, in order to include variation due to any possible hysteresis in the performance of the gauge. Figure 34 shows a plot of the known torque with respect to the measured voltage amplified across the strain gauge bridge output. For each measurement the difference between the best fit line values and the measured values was calculated. The variations from the best fit line were analyzed for normal distribution in order to justify the use of standard deviation in estimating the error in converting voltage to torque using the linear regression line formulae. Using MS Excel statistics on the set of differences (variations of the measured data from the best fit line), the skew and kurtosis were found to be -0.89 and 0.071 respectively. These two values are consistent with the assumption of a normal distribution of errors about the linear calibration curve. Error in the torque measurement was then calculated from the standard deviation of this data set to be $\pm .0085$ Nm.

The conversion of voltage to torque is thus calculated using the formula

$$\tau = \left(0.744\frac{\mathrm{Nm}}{\mathrm{V}}\right)\mathrm{V}_0 - 2.263 \ \pm .0085\ \mathrm{Nm}, \tag{5.1}$$

where V_0 is the amplified voltage across the strain gauge bridge. The linearity of this calibration curve (shown in figure 34) was expected due to the response characteristics of the Omega torsion gauges used.

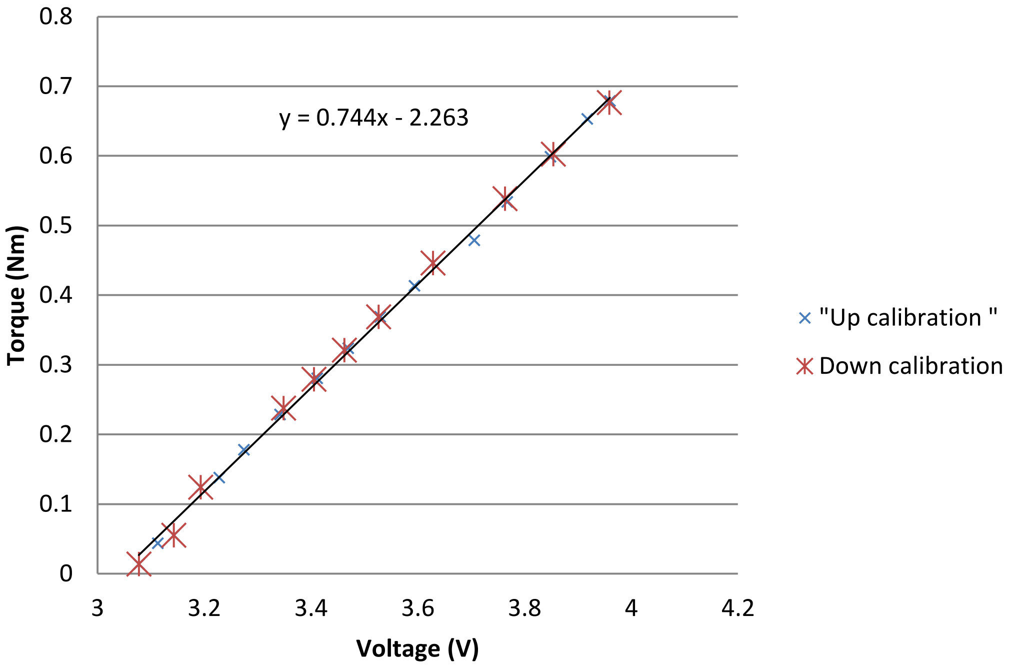

Figure 34 Torque vs. Voltage

5.2 Optimal Load Resistance

For the system set-up parameters noted in Table 5, the harvester was operated for variation in load resistance as specified in Table 3. The plot of Figure 35 shows the variation in power output due to changes in load resistance. The results indicate that the optimal ratio of system resistance to load is 1 where the system resistance is 60 ± 0.05 Ω. The error bars in Figure 35 represent the standard deviation of the mean for three different trials of the power output averaged over 5 seconds of device operation at 8.38 ± 0.06 Hz. Horizontal error bars were too small to observe as they represented only a small fraction of the load values on the order of 10^{-3}.

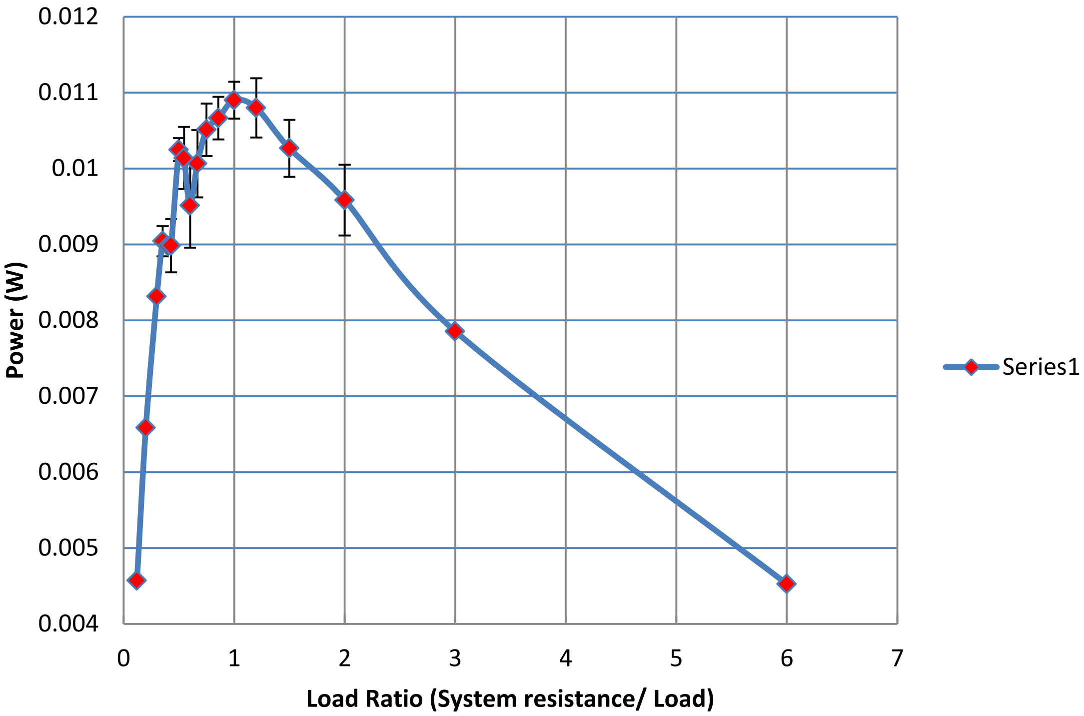

Figure 35 Optimal load for power production (horizontal error bars negligible)

The results here are consistent with De Marqui and Erturk [24] in that the optimal power is found where the load to system ratio is 1. For this reason, during the remaining experiments where performance of the harvester was examined, the value of load resistance was maintained at 60 ±.05 Ω. The intention is not to prove that this resistance value is optimal for all cases. Rather, it is done to provide some justification for the use of a constant load, because the optimization of load for each set up case is beyond the scope of this investigation.

5.3 Performance Evaluation

The harvesting device was set up and operated for varying wind speed and foil chord while all other variables were held constant (table 5). It was not possible to produce wind speeds as specified by the experimental set-up (table 6) because the motor driving the fan in the wind tunnel was not stable at exactly those values. Consequently, the motor was adjusted to get as close as possible to the prescribed values. The wind speeds actually tested are shown in table 7 along with the foil chord sizes and the dimensionless frequency resulting from those combinations, where N/A is written on the table there was no observed performance of that airfoil at that windspeed. Three additional experiments were performed, in order to investigate the reduced wind speed of 2.24 m/s for smaller airfoils, as there was evidence (from observation) that they could operate at this reduced wind speed whereas the larger foils could not.

Five seconds of Torque Voltage (500 Hz sample rate), load voltage (500 Hz sample rate), and 5 seconds of video imaging (420 fps) were recorded for each test. Examples of the data will be shown, as well as graphs representing quantities and relationships of interest, these results will be discussed.

Table 7 Actual testing values for performance evaluation and matrix of *f**

	Wind Speed (m/s)					
chord (mm)	2.244	3.111	3.621	4.335	5.1	6.324
30	0.116	0.085	N/A	N/A	N/A	N/A
40	0.154	0.114	0.096	0.080	0.069	0.056
50	N/A	0.137	0.116	0.099	0.084	0.068
60	N/A	0.162	0.139	0.116	0.099	0.081
70	N/A	0.189	0.163	0.136	0.117	0.095
80	N/A	0.217	0.184	0.154	0.133	0.107

5.3.1 Power Performance

Image samples are provided for the 70 mm foil operating at 4.3 m/s (figure 38). Examples of voltage output and frequency spectrum (figure 39) are provided for the 70 mm foil at 3.621 m/s. Note that the first peak in figure 39 represents the forced and damped (due to the power take off) primary bending mode frequency of the beam while the second peak at 5 times this frequency is likely associated with the power take off. Instantaneous torque voltage is shown, along with instantaneous load voltage (Figure 37) to compare the heaving oscillation cycle with the voltage output across the 60Ω load. Other data are presented as required.

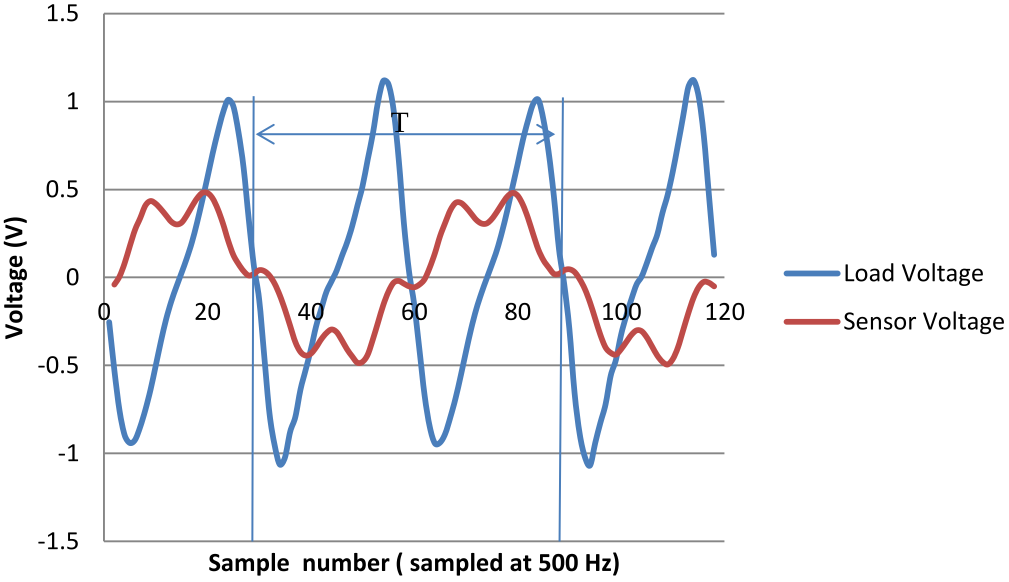

Figure 36 Sample of Load and torque sensor voltage over a cycle

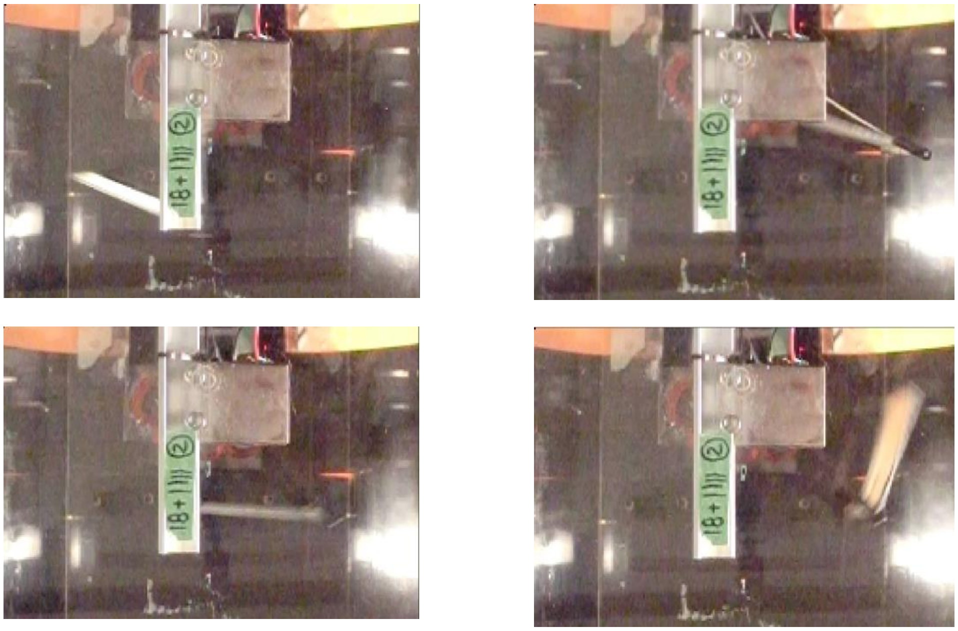

Figure 37 Frames of image data for 70 mm chord at wind speed of 4.3 m/s, images taken at 0, 1/8T, 1/4T, and 3/8T where T indicates the period of heave oscillation

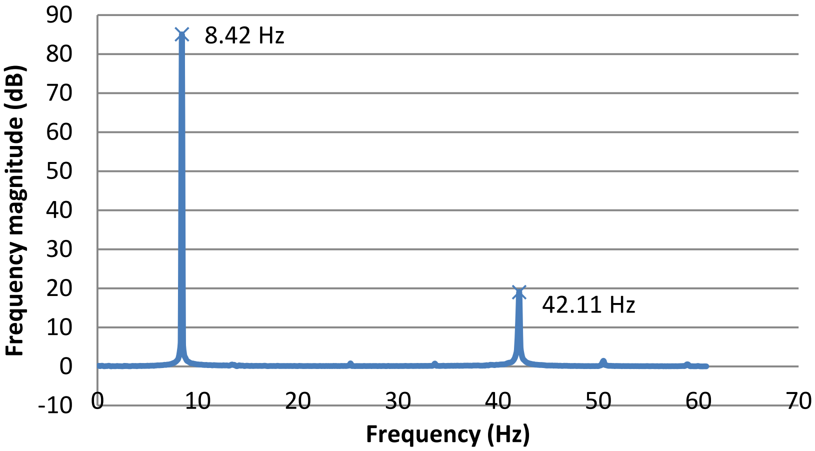

Figure 38 Frequency analysis of the torque data showing primary frequency peaks below 60 Hz

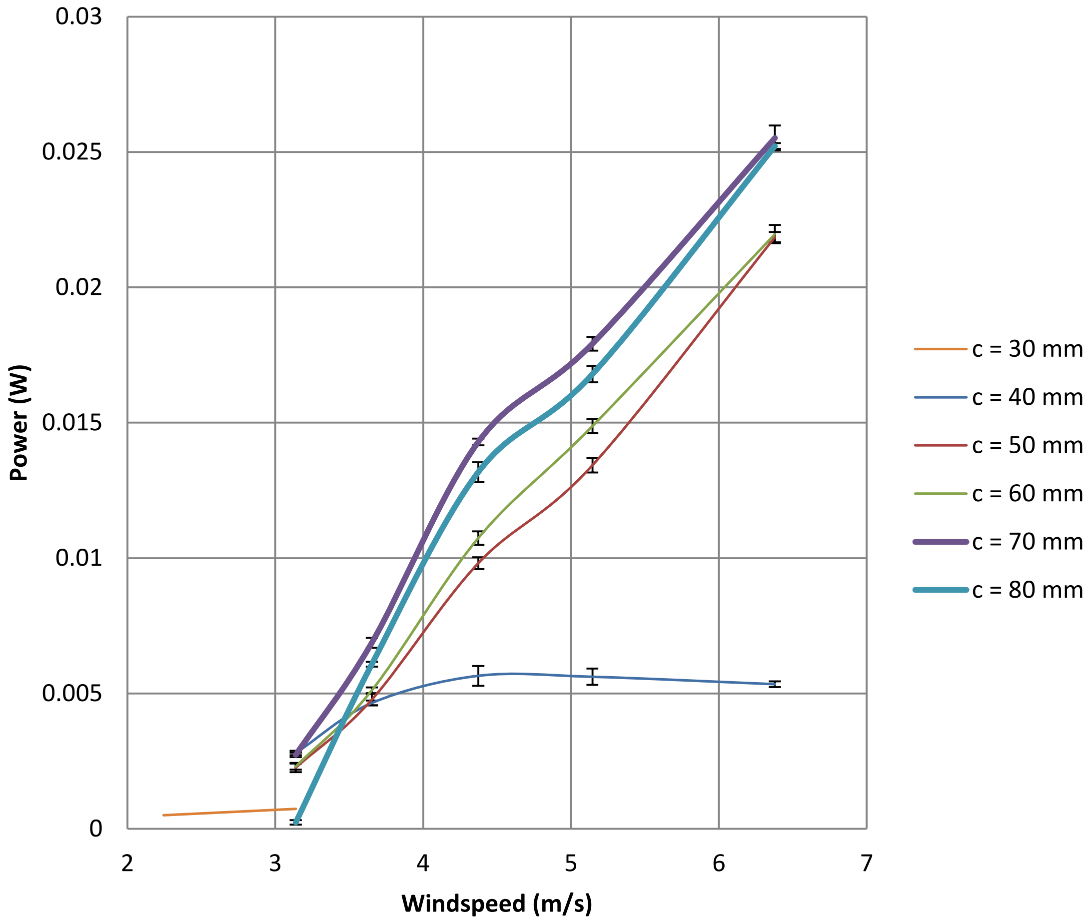

Figure 39 Device power output for different foil sizes

The highest power output achieved over the results for averaged power (figure 39) was 25.51±0.46 mW for the 70.0±0.5 mm foil at a wind speed of 6.30±.05 m/s. The performance of the foils varied over the range of wind speeds. At the lowest wind speed tested (2.2 m/s) only the 30 mm and 40 mm foils were self-starting. At 3.1 m/s wind speed all foils were self-starting though the 80 mm foil took approximately 40 s to reach steady state at this wind speed, the 70 mm foil self-started more quickly than this (time not recorded), but was slower than the smaller foils to achieve steady-state oscillation. All of the foils except the 30 mm airfoil readily began oscillation at the higher wind speeds as soon as the fan in the wind tunnel was switched on.

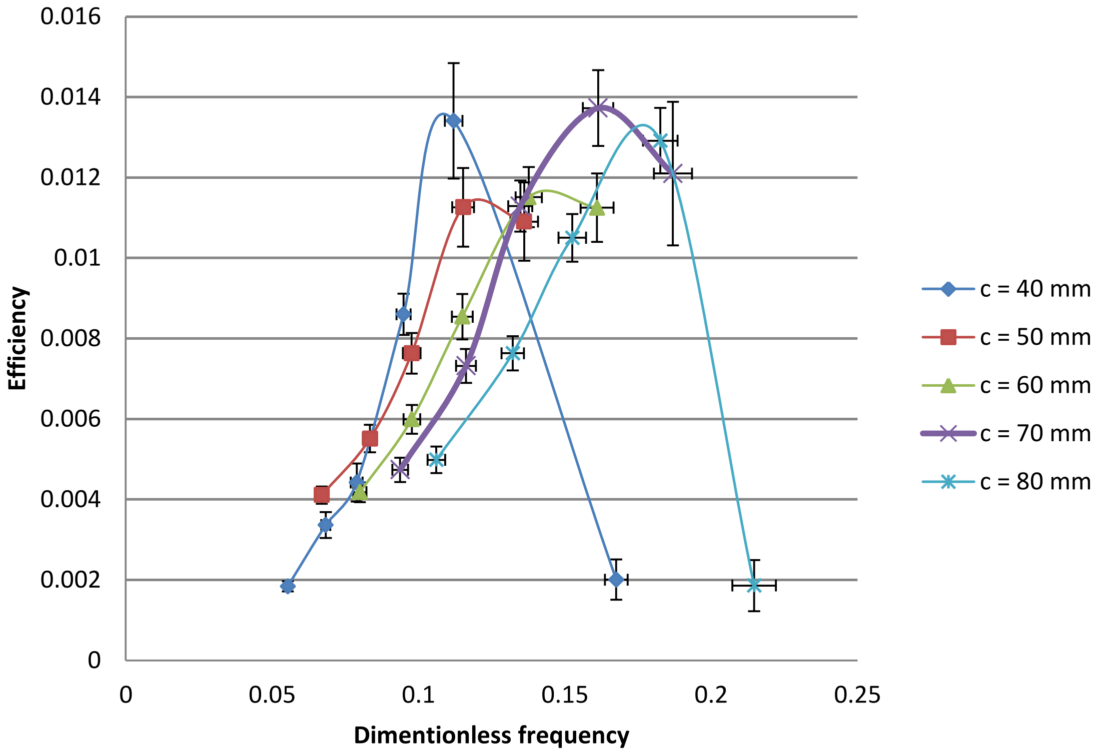

Figure 40 Device efficiency as a function of *f**

The highest efficiency (plot of efficiency for different foil chords shown in figure 40), a value of 1.37 ± .09 % at the dimensionless frequency of 0.161 ± 0.005, was observed with the 70.0 ±0.5 mm foil operating at 3.65±0.05 m/s. The operating conditions for this trial are summarized in Table 8.

Table 8 Operating conditions for maximum efficiency trial

d_o (mm)	Θmax (^{0})	f (Hz)
61.15±1.67	86.6 ±1.2	8.42±.06

The maximum efficiency across all the foils tested was found between f^* of 0.112 and 0.182. The dimensionless frequency and operation conditions of this optimal case suggest an agreement with the results of Zhu et al. [18], in which an optimal energy harvesting case is presented for $c/d_o = 1$, $\theta_{max} = 90^o$, and a dimensionless frequency of 0.15. The results here are compared with these conditions in Table 9. Another experiment was carried out to consider the optimal *f** for a different set-up condition using the 70 mm foil. This test was conducted not only to see whether the trend in *f** holds in another set-up, but also to increase the power take-off of the system using a larger magnet (0.75 inch diameter) to see if more power could be pulled out of the system. This test is described and discussed in section 5.3.1.

Table 9 Comparison of highest-efficiency trial with operating conditions from Zhu et al.

	d/c (mm)	Θmax (^{0})	f^*
This study	0.874 ± .027	77.63 ±1.85	0.161 ± 0.005
Zhu et al.	1	90	0.15
% difference	12.6 ± 2.7	13.7 ±.05	7.33 ± 0.23

The average torque value for all cases varies approximately linearly with the power output, as shown in Figure 41. The maximum average torque of 0.458 ± .009 Nm correlates with the maximum averaged power. This result indicates that for a relatively constant frequency of vibration between 8.3 and 8.8 Hz (Figure 43), the amount of power extracted from the device can be approximated from the torque value via a linear relationship for a given power take-off. This has significance in that, as the device increases its heave displacement, causing the root moment to increase, the device extracts more power in a direct relationship to this root moment. In this way, the linear relationship is a measure of the “evenness” of the power extraction over the range of motion observed. The slope becomes, therefore, a measure of the ratio of torque to power. In this situation the calibration curve is developed as a linear regression of the entire data set for torque and power and is provided as

$$\tau_{av} = (14.84\frac{Nm}{J}) * P_{av} + 0.0914\ Nm$$

Also shown for consideration are the power and torque curves with respect to wind speed in Figures 39 and 42, respectively.

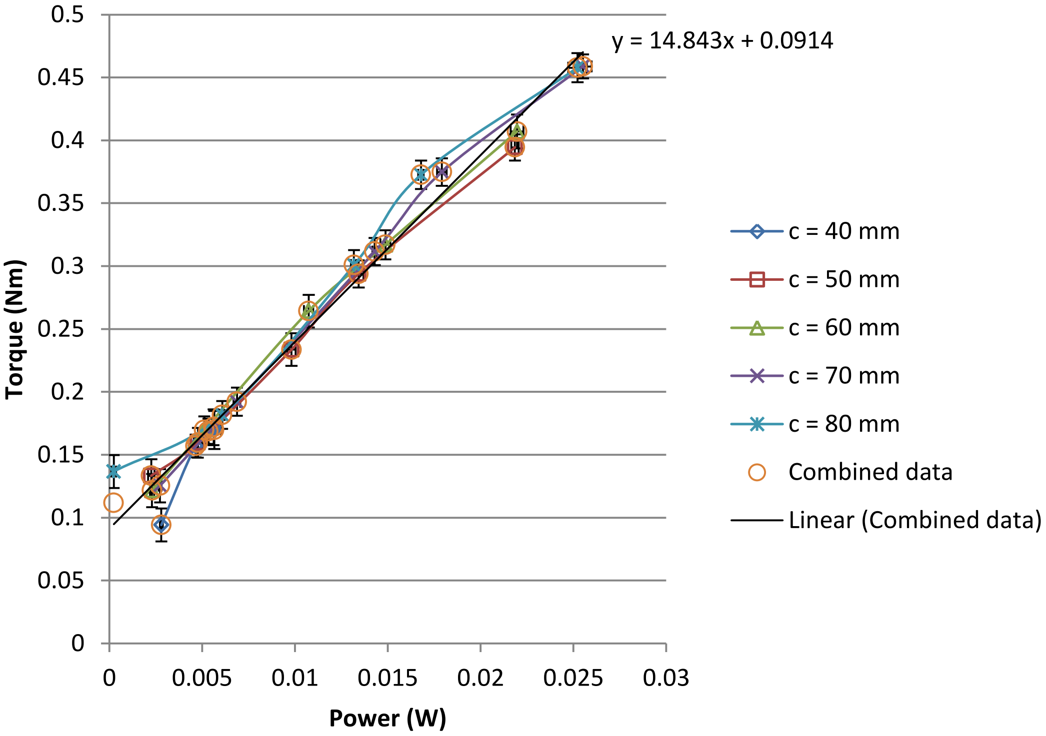

Figure 41 Power vs. Torque for the entire data set

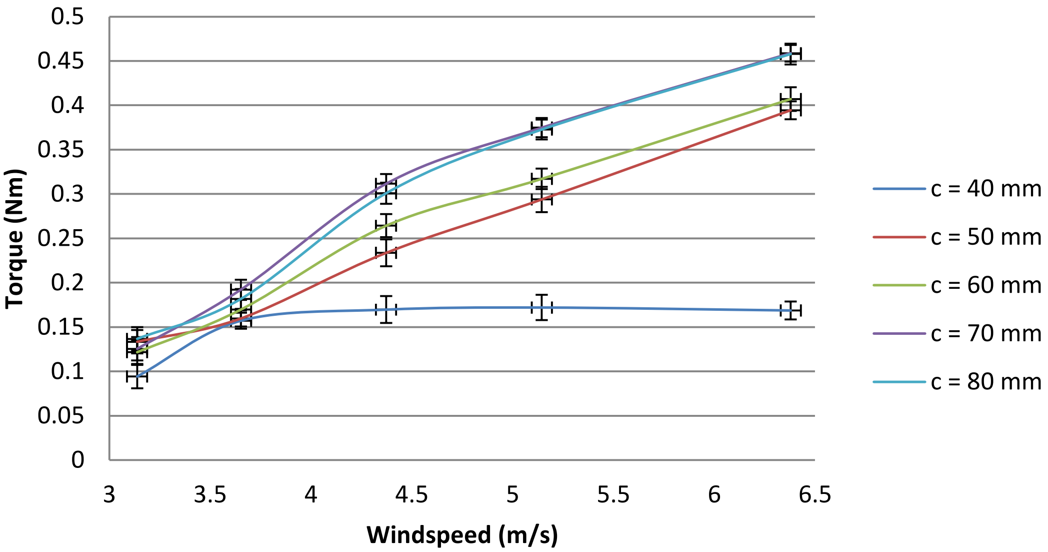

Figure 42 Torque vs. Wind speed

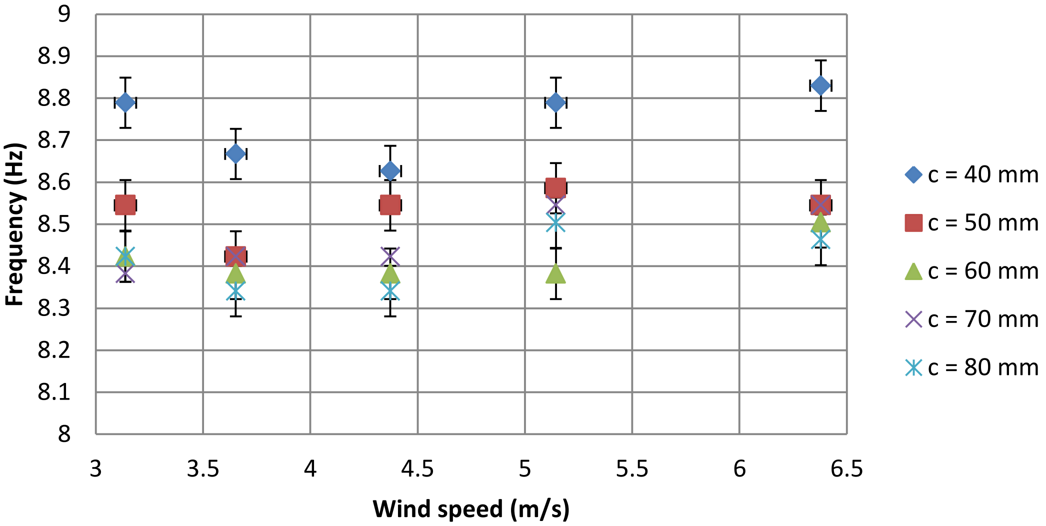

Figure 43 Spread of heave oscillation frequencies for different foil sizes

5.3.2 Operation Dynamics

For f^* to increase, either the chord must increase or the wind speed velocity must decrease for constant operating frequency f, from eq. 1.10 (Refer to Figure 44 for the spread of f remaining relatively constant for the trials shown here). To connect f^* and device performance the windspeed chord are considered in the flow dynamics of flutter. Initially, it is proposed that the time it takes for a stall vortex to develop and shed downstream is inversely proportional to wind speed and directly proportional to the size of the foil. This effect is observed in studies of Strouhal number on flat plates [10]. Because the frequency of device operation is relatively constant, in order for the vortex to generate and shed during one half-cycle (between maximum heave positions) it needs to go through the process of vortex generation and shedding at a speed of 1/2T. If the leading edge vortex develops too slowly it is forced to shed by the changing direction of the heave motion rather than by convection due to the vortex propagation in the foil wake. If it generates too fast, the vortex sheds too soon, shedding before the device can complete its motion between maximum heave positions. This timing can be tuned (so long as the device remains at relatively constant operating frequency) the windspeed and/or the chord length. Considering the strong pitching moment caused by the stall vortex described by Carr et al. [29] helps to explain the role of this timing in the performance of the flutter. The strong pitching moment generated via the stall vortex maintains the angle of attack to the wind which drives the heaving force on the foil. If the vortex generation and shedding does not match the motions of the foil, efficiency is lost due to sub optimal flow dynamics. The importance of this timing can be observed in results reported by Zhu [18] where, for a prescribed motion of an airfoil at $Re = 1000$, he provides sequences of the vortex shedding dynamics (developed through numerical methods) for different f^* values. For $f^* = 0.06$ it was shown that the leading edge vortex develops too quickly and sheds before the heave amplitude reaches its maximum. Considering Carr’s description of dynamic stall [29] implies that the pitching moment maintaining the angle of attack (caused by a strong stall vortex) drops off before the end of the heaving motion, leading to a loss in potential power generation. For an $f^* = 0.2$, Zhu shows the stall vortex generating slower relative to the heave period so that the vortex is forced to shed (by changing heave motion) before it reaches maximum strength, again, losing potential in generating power. For the optimal $f^* = 0.15$ Zhu shows the stall vortex being shed at its maximum strength and coinciding with the point of maximum heave, leading to a loss of moment very close to the time when the change in heave direction would induce a shedding of the leading edge vortex were it not shed naturally due to convection.

For the results here there is a unique opportunity, due to the lack of stiffness on the pitching axis of the foil, to observe the effects of a fluttering device where the pitching angle leading to an angle of attack which drives the heave motion, is mostly driven by the effects of dynamic stall (with the exception of possible “swinging” of the foil). The results for the 40 mm chord airfoil tested (Figures 44, and 46), show that as the f^* decreases the phase relationship between the heave and the angle of attack becomes increasingly negative, meaning that the point where $\theta = 0$ in the cycle moves to the left in the time line relative to the datum of the maximum heave position (this trend of reducing phase with decreasing f^* can also be seen with the other foils, the pitching angle for the 70mm chord tests is shown in figure 45 for comparison). For the 40 mm chord airfoil tests, as *f** decreases, there is an *f** value where maximum angle of attack (Figure 47) beyond which the maximum angle of attack is reduced, implying a reduction in the moment sustaining the high angle to the wind. The changing of this phase value as *f** changes shows that for slowly developing stall vortex--for high *f** values--the moment is maintained for a longer interval that leads to a pitching angle that is maintained past the maximum heave position where the vortex is shed due to changing heave motion. As the *f** reduces, the shedding occurs more quickly. Therefore, the pitching phase gets closer to coinciding with the point of maximum heave. For very low *f** ~ 0.055, the zero-pitch point occurs before the maximum heave position, as can be seen in figures 44 and 46. It should be noted also that in order to observe these effects it is important that the device is experiencing enough damping to effect observable change in the motion of the heave, for without effective damping the device becomes divergent for even small “pushes” per cycle. (A “push” is defined as any force in the direction of heave motion per cycle.)

For the system set up with 0.5 cm diameter magnet there appeared to be a strong reactive response, with respect to angle of attack and power production, for the 40 mm foil, likely because the smaller foil has less power for the same *f** and operating conditions than a larger airfoil at the same pitch angle, likely due to the larger surface area interacting with the flow. For increasing flow speed there was an attenuation of the power output of the 40 mm foil below *f** of 0.1, implying that, with large enough damping provided by the power take off, as the wind increases the power output will decrease, leading to a damping of motion which protects the structure from damage in high wind speeds. The effect of this damping can be observed in the 40 mm foil for the highest wind speed case with the power output to the load disconnected. The displacement of the 40 mm foil at the 6.3 m/s wind speed with damping is measured at 99.5± 3.3 mm and without damping at 216.4 ± 4.5 mm. This shows a decrease in heaving amplitude of approximately 117% by coupling the device with the power take off. The fact that the highest amplitude motion for the damped 40 mm foil was not at the highest velocity flow speed (highest damped heave displacement for the 40 mm foil was 104 ± 3.4 mm at 4.3 m/s flow velocity) is evidence of the potential of this device, if the power take off is scaled correctly, to have a passive self-governing capability. Figure 48 shows the displacement for d_o and Y (Y is the total heavwise distance traversed by the device). From Figure 47 it can be seen that for each airfoil, other than the 40 mm foil, there comes a point where, as the airspeed is increased, the power in the foil motion apparently overcomes the damping that would attenuate the angle of attack and the heave (figure 48) continues to increase with increasing wind speed (heave being directly related to torque which is linearly related to power output). To validate the postulate that the damping plays a role in this divergence of maximum angle of attack, leading to an attenuation in heave, the results of the 70 mm foil under increased power take off are described in 5.4.1. From Figure 47 a trend can be seen where, over all of the foils tested, and for the measurements of angle of attack that don't seem to diverge at increased wind speeds (i.e. the 40 mm foil, presumably due sufficient damping in the system), there is a trend toward a maximum angle of attack in the region around the f^* of 0.15 (figure 48). This further supports the existence of an optimal dimensionless frequency for energy harvesting operating in this harvesting design.

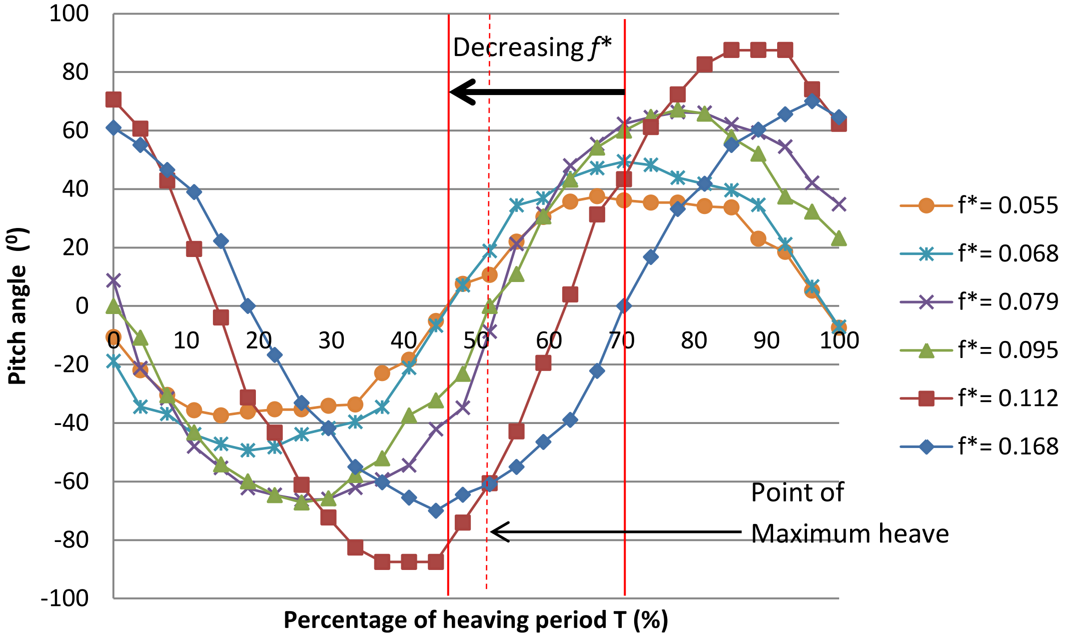

Figure 44 Changing foil angle relative to the global wind direction presented over a full cycle of motion for the 40 mm foil

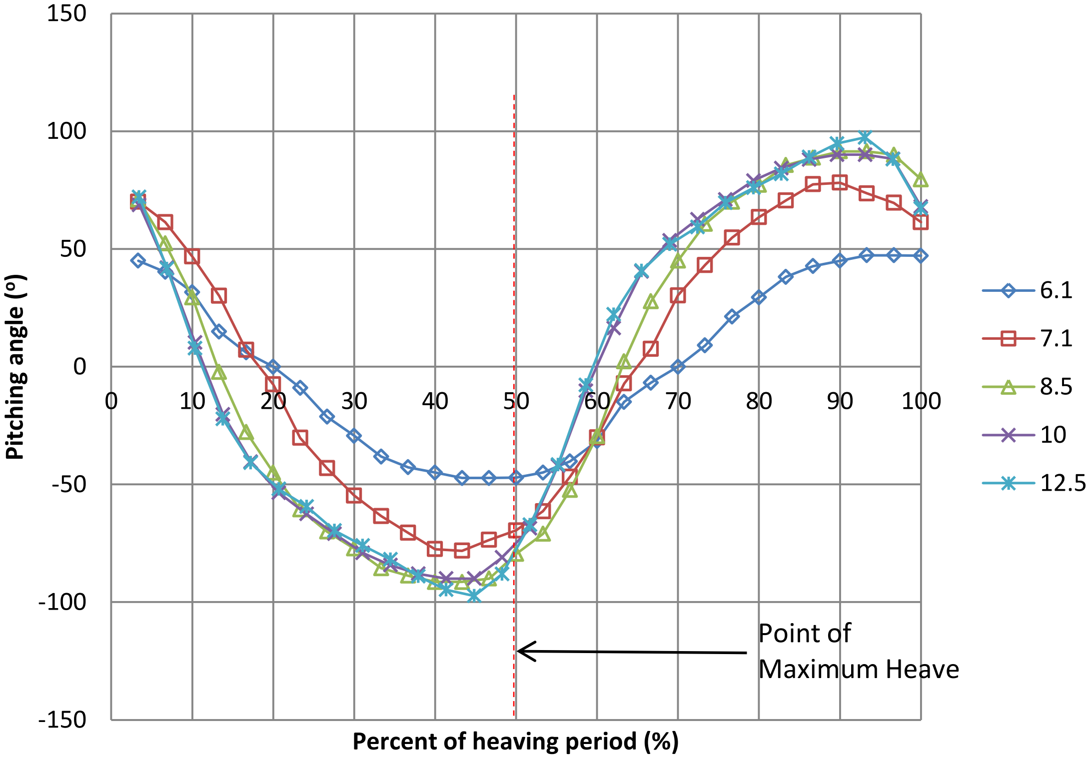

Figure 45 Pitching angle change relative to heave cycle for the 70 mm foil shown for comparison

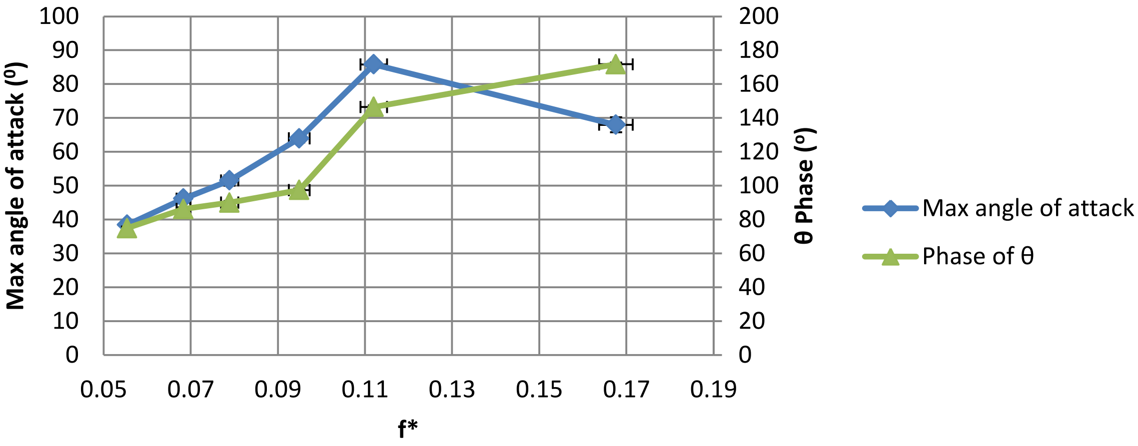

Figure 46 Pitching phase and angle of attack for the 40 mm foil

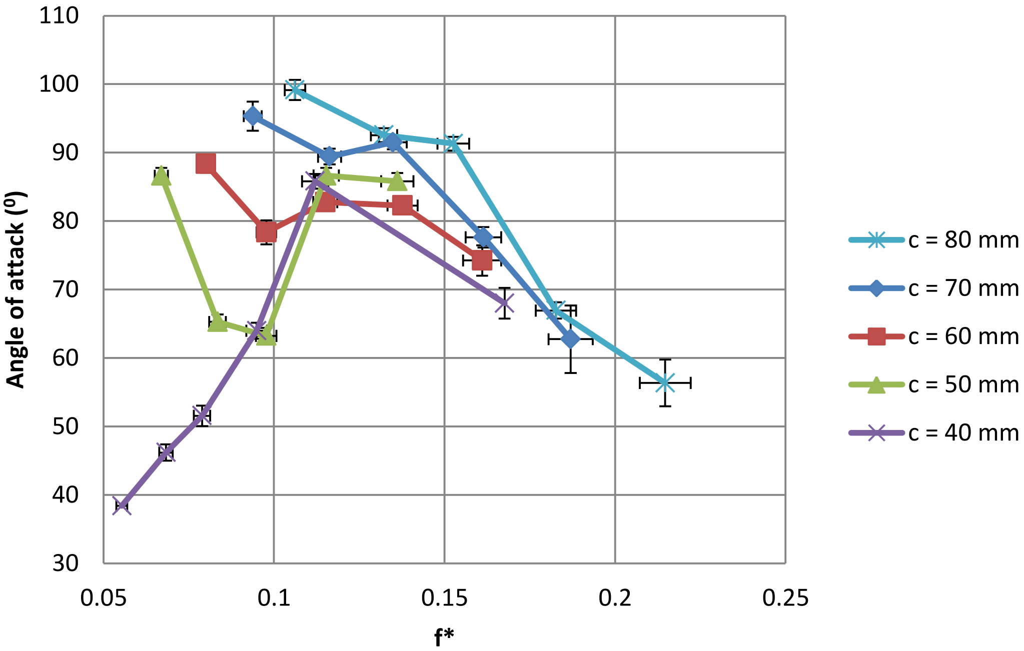

Figure 47 Maximum angle of attack vs. dimensionless frequency for experiments on different foils

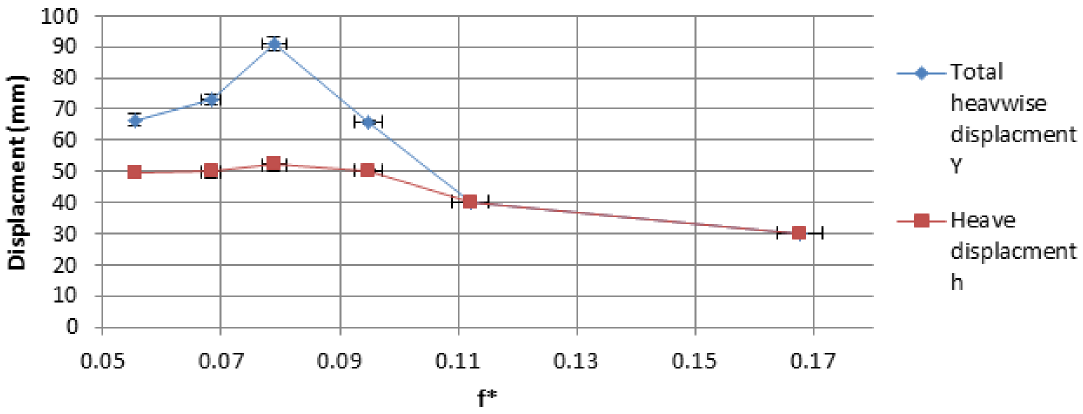

Figure 48 Heavwise displacement (*Y* and *h*) for the 40 mm foil chord

5.4 Additional Investigations

Two experiments were added as a response to the previous results. The evidence suggesting that the optimal *f** lies in the region surrounding 0.15 (as defined by Zhu [18]) is clear. A choice was made to use the airfoil which yielded the highest power output and to change the set up and power take off to observe a similar outcome. The second experiment in this section looks at the effect of changing the angle of the device to the wind. This is an important factor to consider for a harvester which is subject to variable wind directions, because this device does not automatically yaw to align itself with the prevailing wind. For this experiment, the device was operated at a particular wind speed and set-up condition, and the performance was observed for changing device angles.

5.3.1 Confirmation of Optimal Dimensionless Frequency and Phase Relationships

For this experiment the set-up of the harvester was changed to increase the damping in the power take off. To do this the magnet diameter was increased from 0.5 to 0.75 inches. Because the added weight of the magnet reduces the resonant frequency of the heaving motion, a thicker beam of 0.5 mm was used and the length of the beam was increased by 10 mm. This resulted in an operating frequency of 9.62 ± .11 Hz over all tested wind speeds. With the added mass (larger magnet and beam) the primary mode bending frequency reacts less to changing windspeeds and flow dynamics due to its inertia than the previous lighter set up.

Table 10 Set up values for the increased power take off

l (mm)	*t* (mm)	Gap (mm)	Magnet diameter (in)	*Xm* (mm)	*R* (Ω)	*c* (mm)	*U* (m/s)
150	0.5	0.5	0.75	70	60	70	Varied

The 70 mm airfoil was tested at 7 different wind speeds as shown in Table 11. Data was gathered in the same way as the previous experiments.

Table 11 Experimental plan for testing 70 mm airfoil

	Wind Speed (m/s)						
Chord (mm)	3.65	4.17	4.73	5.20	5.71	6.27	6.74
70	0.186	0.162	0.143	0.130	0.118	0.107	0.099

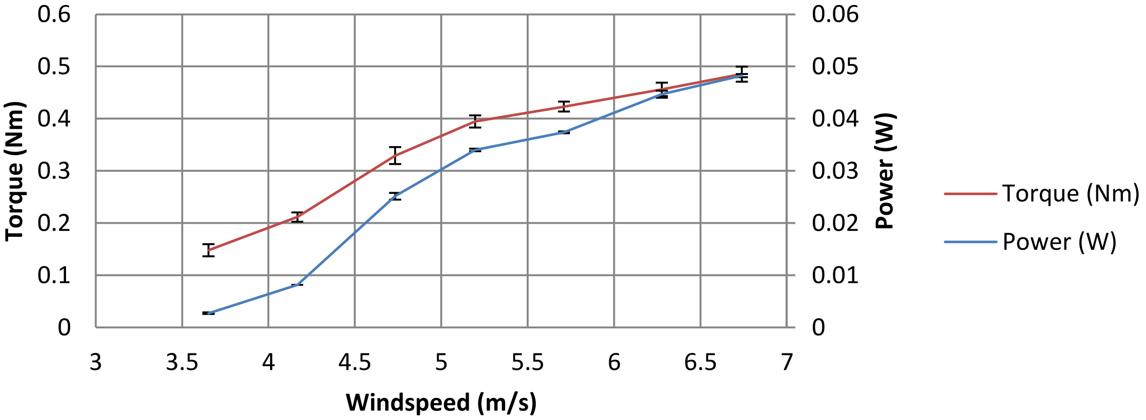

Figure 49 Power and torque curves vs. wind speed

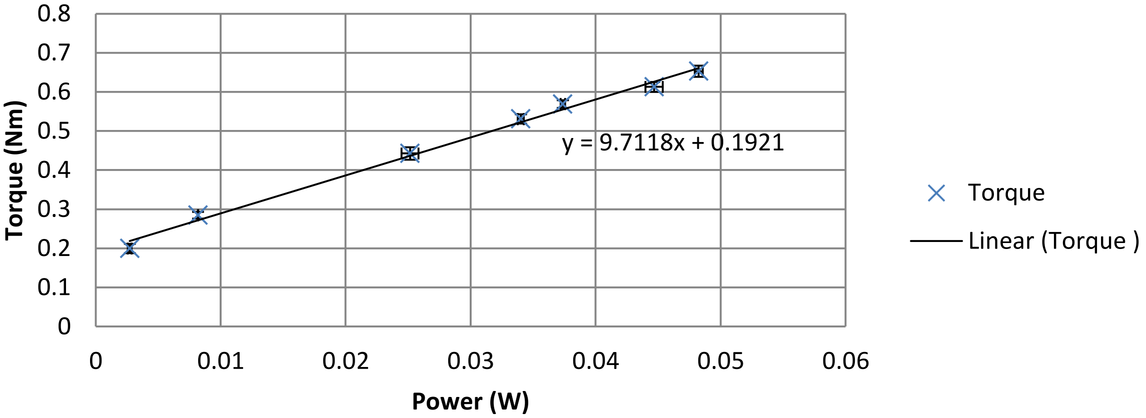

Figure 50 Torque vs. Power graph, showing linear correlation

The highest power output achieved was 48.25 ±0.03 mW for the 70.0±0.5 mm foil at a wind speed of 6.74 ±.05 m/s. The device was self-starting for all tested wind speeds. Maximum averaged torque of 0.049 ± 0.014 Nm corresponded to the maximum power. Consistent with the first set-up, a strong linear correlation between Power and Torque was found over the range of wind speeds tested (shown in figure 50), with a linear relationship described by

$$\tau_{av} = (9.712\frac{Nm}{J}) * P_{av} + 0.1921\ Nm. \tag{5.2}$$

This result helps to confirm the performance of the device over varied power take-off levels. Comparing the two linear curves shows that this power take-off set-up with the larger magnet shows an improvement in power take-off over the range of wind speeds. The power output of the second device shows approximately an 80% increase in maximum power output over the power output of the first set-up at the same torque value (interpolated from torque power curve). This increased power is likely due to a combination of factors. First, the increased operation frequency of ~ 9.5 Hz yields higher velocities. Second, with the increased magnet diameter, there is a stronger magnetic field being passed over the coils. The device's power take off in this set-up for the 70 mm foil is also being matched more closely with the power available in the wind so that the device is not diverging with increasing wind speed. Rather, it is being constrained to drive the power take off with greater force. The trend for maximum angle of attack reaching a local maximum at a *f** value surrounding 0.15 (figure 51) is repeated here as it was for the experiments in the previous tests, although, as predicted, the trend for divergence of the angle of attack with increasing wind speed is not seen here, figure 52. This is presumably due to the increased damping as was discussed in 5.3.

The results for this case also show a clear trend of decreasing phase of the pitching motion with respect to the heave motion (figure 52). The power for the current experiment begins to level off as *f** comes close to 0.1. This suggests a close similarity to the performance of the 40 mm foil in the first set-up. A reasonable prediction would be that after *f** of 0.1 the 70 mm foil with the new set up will begin to attenuate its power output and correspondingly its heave amplitude and torque, which would protect the device in high wind speeds. This should be tested to be sure that it indeed is the case for the higher damping with the 70mm chord, although the trend in the results is already observed to be consistent with what was seen in experiments with the 40 mm chord.

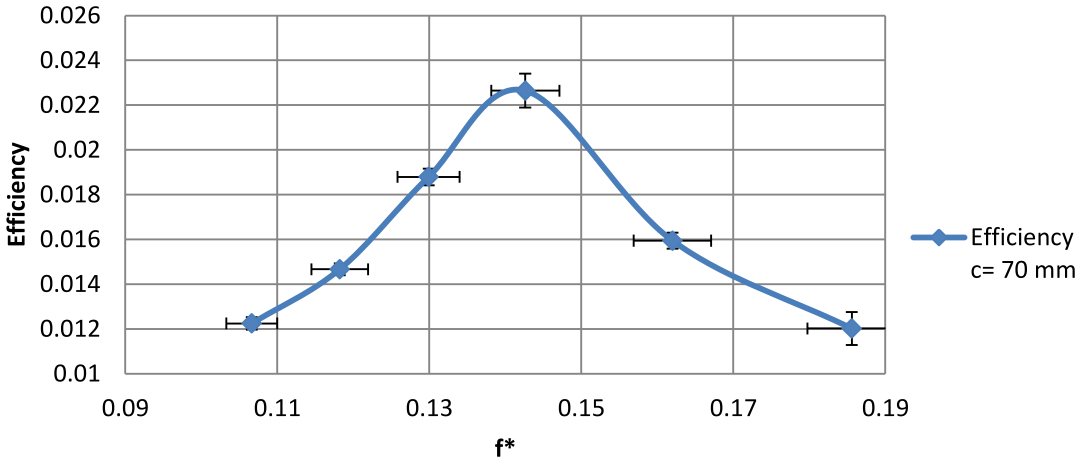

Figure 51 Efficiency vs. dimensionless frequency for the 70 mm airfoil with increased power take-off.

The results of this trial (Figure 51) showed peak efficiency with a maximum value of 2.26± 0.76% at a dimensionless frequency of 0.143±0.004. This result corroborates the evidence of an optimal *f** surrounding 0.15. The results for pitch angle (Figure 52) further support this by showing a broad peak with a maximum value of 69.28 ± 1.27^{o} at a dimensionless frequency of 0.130 ± .004. For the results shown here, it appears that the maximum efficiency coincides closely with the maximum pitch angle. This is reasonable, considering that in order to maintain a strong pitch angle over a heave cycle; a strong pitch moment is needed. This relates to an optimal stall vortex generation as described earlier. From this test it appears that the best efficiency case occurs for a phase relationship of 135.46 ± 0.42^{o}. As with the previous test, however, there is not enough data to characterize fully the efficiency peak in order to show an exact value for optimal *f**. There is nevertheless enough information to show a similarity amongst all tests that indicates peak efficiency and maximum pitch angles surrounding *f** of 0.15. Figure 53 shows the pitch angle over a cycle of heave for the different windspeeds tested. The same trend in reducing phase with reducing *f** and reactivity of the maximum pitch angle is seen here as it was with the previous description using the 40 mm chord airfoil. The values of phase and maximum pitch angle are shown in Figure 52.

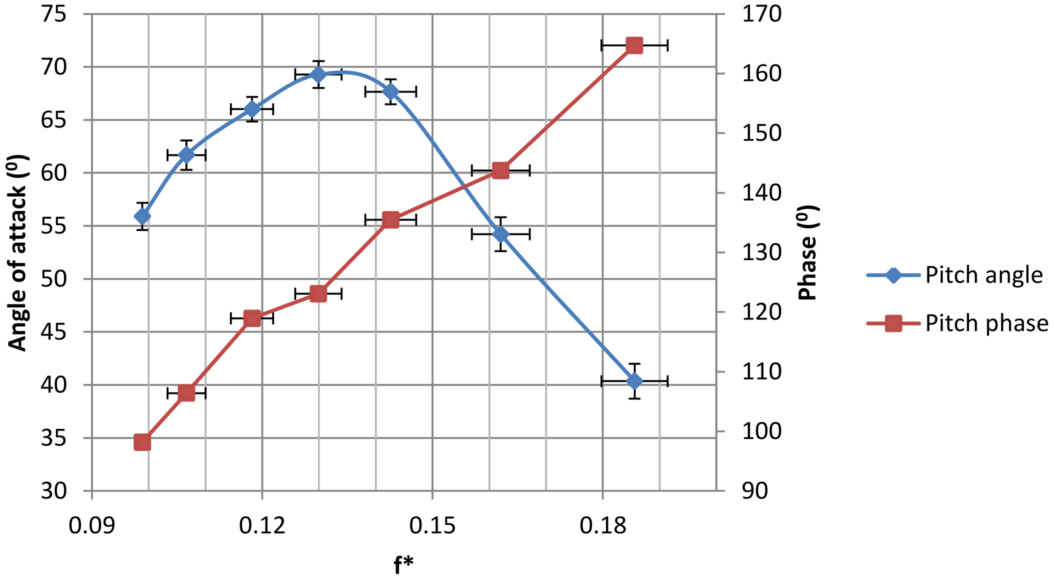

Figure 52 Maximum pitch angle and pitch phase angle (with respect to heave) vs. dimensionless frequency

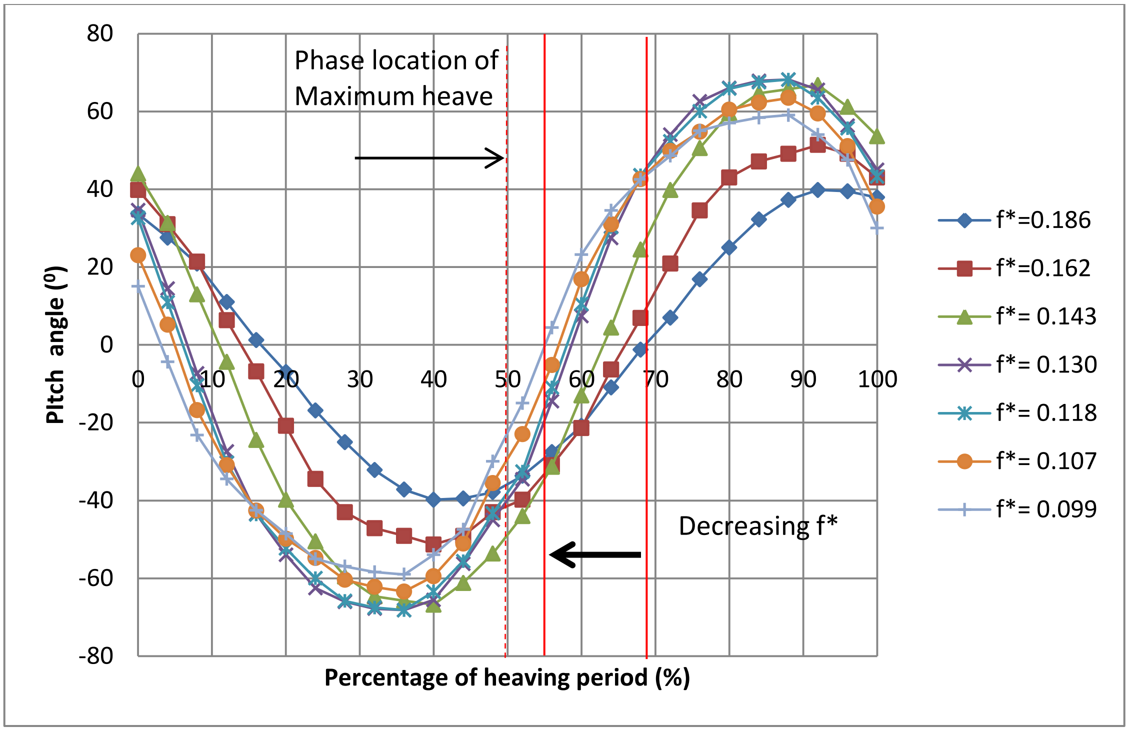

Figure 53 Angle of attack for different *f over a heaving cycle**

5.3.2 Changing Device Angle to the Flow

Four experiments were repeated 3 times each to investigate the ability of the device to generate power at a varied angle to the wind. The set-up conditions are the same as described in 5.3.1, with the only change being alignment of the device at 4 different angles: 0, 6, 12, and 22 degrees. Images of the angled device are shown in Figure 54, and the power output vs. angle is shown in Figure 55. The maximum angle that could be used while still maintaining a reasonable distance--a chord length--from the side wall of the wind tunnel was 22 degrees.

Figure 54 Changing angle of the harvester to the wind for 6, 12, and 22 degrees

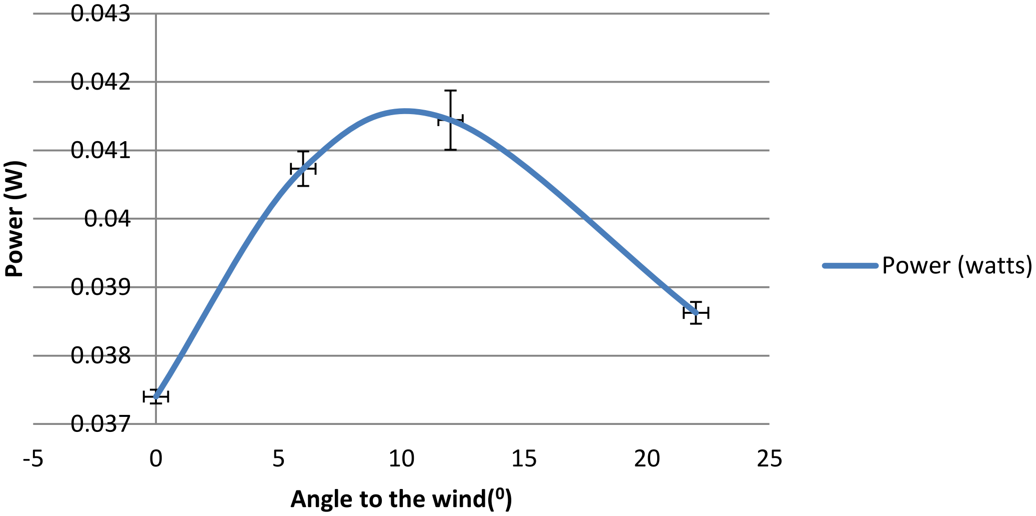

Figure 55 Power as a function of changing wind angle

The results show that there is an increase in power for an angled device from the zero degree condition showing a maximum power output of 42.44 ± 0.43 mW at an angle of 12.5 ± .5^o to the wind direction. This is unexpected, although it could be due possible interactions with the device at the wall of the tunnel. Nevertheless, the results reported in Figure 55-demonstrate that even a small change in the angle results in an increase in the power output. The reasons for this could be due to the effect of the support structure on the wake, although this is difficult to observe without a full flow visualization capability, which would be an important addition to this and all the experiments performed so far.

From a performance standpoint, it is evident that there is no substantial loss of power associated with the angle changes that were made, so it is, at least for these experimental conditions, possible to conclude that the device does not lose significant performance for angles off the wind up to 22 degrees. This result supports a contention that the device is “robust” with respect to wind direction within the range tested. It would be useful to investigate the 360-degree performance of the device so that appropriate choices could be made with respect to arrangement of harvesting arrays for taking advantage of the full spectrum of wind directions from all horizontal and vertical directions.

Chapter 6: Conclusions and Recommendations

6.1 Conclusions

An energy harvesting device driven by aero elastic vibration has been designed and tested for performance under specific operating conditions. The device was designed to consider low cut in wind speed of 3 m/s, simplicity so that there are few parts of low complexity and manufacturing requirements, as well as be robust to withstand heavy weather conditions. The device was also constructed to reach power outputs on the order of 10’s of miliwatts in order to compare with current energy harvesting devices using aeroelastic vibration. The device was tested to observe the performance changes due to dimensionless frequency f^* by way of observing the effect of varying chord length and wind speed for particular set up conditions. For the first system set up parameters of table 5 the results show that the harvester reaches its maximum power output of 25.51±0.46 mW for the 70.0±0.5 mm airfoil at a wind speed of 6.30±.05 m/s (figure 40). The highest efficiency case for this set up was found to be 1.37 ± .09 % at the dimensionless frequency of 0.161 ± 0.005with the 70.0 ±0.5 mm chord airfoil operating at 3.65±0.05 m/s (figure 41). The device operated between 8.3 and 8.9 Hz showing a trend of reducing frequency for increasing chord length (figure 43). All airfoils tested were self-starting for windspeed velocities exceeding 3 m/s.

A description of the effects of dynamic stall vortices on the performance of the device was presented and used to understand the changes in performance observed in the results. A qualitative description of the effect of windspeed and chord on the optimal conditions for energy harvesting was provided in section 5.3.2 where reports of Carr et al. [29] and

Zhu [18] are compared to the results. It was observed that the impact of the dynamic stall vortex, generation and convection downstream, was most effective for energy harvesting (considering efficiency) when the dimensionless frequency *f** was in the region surrounding 0.15 corroborating results by Zhu[18].

Two experiments were added as a response to the results in section 5.3.1 and arguments of 5.3.2. The first was to change the set up parameters of the device (most notably the magnet diameter was increased in the power take off) and test it over a range of windspeeds with the best performance airfoil, 70 mm chord. Set up parameters of Table 10 were used along with the treatment of table 11. The results show the highest power output achieved was 48.25 ±0.03 mW for the 70.0±0.5 mm foil at a wind speed of 6.74 ±.05 m/s showing an 80% increase in power capacity over the previous set up at the same windspeed. The results of this trial showed peak efficiency of 2.26± 0.76% at a dimensionless frequency of 0.143±0.004. This result further corroborates the evidence of an optimal *f** surrounding 0.15 as reported by Zhu [18]. The results of this trial also support the phenomenon that shows for increasing windspeed the device begins to reduce its rate of increase in power output thereby protecting itself in high wind seeds. This effect was observed for the 40 mm foil, where the power output and torque reduce for increasing windspeed, though more tests need to be done with the 70 mm airfoil to observe a reduction in power output for increasing windspeeds. It is also reported that damping (due to the power take off) plays an important role in this effect. The second experiment was added to observe the effect of changing the angle of the device to the wind. The results show that from a performance standpoint, it is evident that there is no observed loss of power production for angles off the wind up to 22 degrees and that a small increase in power output was observed for angles off the wind up to 22 degrees.

6.2 Recommendations

6.2.1 Design

From previous investigations [31] it was shown that aspect ratios of 5 result in efficiency reductions of up to 30%. For aspect ratios of less than 5 no results are documented though it is assumed that greater losses would be expected. For the current device which has an AR of around 2 for the 70mm chord airfoil , it is reasonable to assume that large losses in efficiency are due to this low AR therefore it is recommended that increasing this aspect ratio may have a favorable effect on the efficiency of the device.

The current power take off results in abrupt changes in power output which means that the damping over a cycle is intermittent. The effect of this intermittent damping on the performance is unknown though it is likely that further refining the design of the coil array to provide a smoother power extraction might improve the power and performance of the device. Losses due to resistance in the 32 gauge wire used to wind the coils could be reduced by increasing the diameter of wire which could also affect power output.

The design is currently at an experimental prototype stage in development. Developing a prototype that could be easily manufactured and installed in a typical operating environment would be a useful next step to observe the performance of the device in real world conditions.

It would be interesting to investigate the use of this device in changing mediums, water for example, and at different scales and flow regimes relating to the Reynolds number. A fluttering energy harvester operating at large scales opens the possibility of servicing larger power requirements. This could require a considerable investment in prototyping though it could show merit in providing alternatives to rotary based power generation.

6.2.2 Experimentation

The optimal load experiment performed showed that the highest power was available where the load matched the system resistance. As the power take off in the device is more closely matched to the power available in the wind it would be useful to revisit the optimal load experiment so that performance may be controlled by adjusting the load on the system. This could provide a tool for tuning a standard device to a given wind speed range.

The results showed that there is potential of this device to self-regulate in high wind speeds. In order to verify this effect experiments should be performed that observe this effect directly for increasing windspeed on airfoils other than the 40 mm one tested. Evidence was shown that suggests the 70 mm airfoil has a trend towards a reduction in power as the wind speed increases though it was not directly observed. Verifying this phenomenon over a range of chord values would mean that devices of this type could be tuned to passively regulate their performance so that they protect themselves from destruction in high wind speeds.

Results showed that the optimal f^* for energy harvesting occurs close to the value of 0.15 as described by Zhu [18]. In order to better characterize the optimal f^* for this device increased experiments surrounding optimal *f** should be performed as the efficiency peaks shown in figures 52 and 41 do not have sufficient data to provide a precise optimal value for *f**.

In order to determine more conclusive evidence for the description of dynamic stall effecting the variation in pitch angle flow visualizations should be performed. Flow visualization could provide a visual record of the timing described in 5.3.2 which would allow designers and scientists to better understand the phenomenon which drives flutter.

Bibliography

[1] R. D. Blevins (1986), *Flow-Induced Vibration*. Malabar, Florida: Robert E. Krieger publishing company Inc.

[2] Theodorsen, T. (1935). *General Theory of Aerodynamic Instability and the Mechanism of Flutter*. Washington, DC: N.A.C.A. Technical Report No. 496.

[3] K. Lindsey (2002). *A feasibility study of oscillating-wing power generators* (Master's thesis, United States naval postgraduate school, Monterey, California).

[4] Dowell, E. H., Crawley, E. F., Curtiss Jr, H. C., Peters, D. A., Scanlan, R. H., & Sisto, F. *A Modern Course in Aeroelasticity*. 1995.

[5] Gerrard, J. H. (2006- reprint from 1965 paper). *The mechanics of the formation region of vortices behind bluff bodies*. Journal of Fluid Mechanics, 25(02), 401.

[6] Li, S., Yuan, J., & Lipson, H. (2011). *Ambient wind energy harvesting using cross-flow fluttering*. Journal of Applied Physics, 109(2), 026104.

[7] Von Karman, T. (1911). Über den Mechanismus des Widerstandes, den ein bewegter Körper in einer Flüssigkeit erfährt. *Nachrichten von der Gesellschaft der Wissenschaften zu Göttingen, Mathematisch-Physikalische Klasse*, *1911*, 509-517.

[8] A. Mallock, (1907) *On the resistance of air*. Proc. Royal Soc., A79, pp. 262–265.

[9] H. Bénard, (1908) Comptes rendus de l'Académie des Sciences (Paris), vol. 147, pp. 839–842, 970–972.

[10]] K. Lam, C Wei (2010). *Numerical simulation of vortex shedding from an inclined flat plate*. Engineering Applications of computational fluid mechanics 4(4), 569-579

[11] C. W. Knisely (1990). *Struhal numbers of rectangular cylinders at incidence*: A review and new data. Journal of fluids and structures 4, 371-393

[12] J. Chen, Y. Fang (1996). *Struhal numbers of inclined flat plates*. Journal of wind engineering and industrial aerodynamics 2(3), 99-112

[13] Sarioglu, M., & Yavuz, T. (2000). *Vortex shedding from circular and rectangular cylinders placed horizontally in a turbulent flow*. Turkish Journal of Engineering & Environmental Sciences/Turk Muhendislik ve Cevre Bilimleri Dergisi, 24(4), 217-228.

[14] Blevins, R. D. (1990) *Flow-Induced Vibration*, 2nd edn., New York: Van Nostrand Reinhold.

[15] Simpson, B. J., Hover, F. S., & Triantafyllou, M. S. (2008, January). Experiments in direct energy extraction through flapping foils. In *The Eighteenth International Offshore and Polar Engineering Conference*. International Society of Offshore and Polar Engineers.

[16] A. Fernandes, M. Armandei (2011). *Passive energy extraction through oscillation of a yawing flat plate operating in a uniform current*. Ocean space utilization, ocean renewable energy, proceedings p 879-886

[17] G. Taylor, R. Nudds, A Thomas (2003). *Flying and swimming animals cruise at a Strouhal number tuned for high power efficiency*. Nature, vol. 425, 707-711

[18] Q. Zhu (2011). *Optimal frequency for flow energy harvesting of a flapping foil.* Journal of Fluid Mechanics. 675, 495-517

[19] Q. Xiao, W. Liao, S. Yang et. Al. (2012*). How motion trajectory affects energy extraction performance of a biomimic energy generator with an oscillating foil*. Renewable Energy, 37(1) 61-75

[20] Anderson, J. M. (1996). *Vorticity control for efficient propulsion* (No. MIT/WHOI-96-02). MASSACHUSETTS INST OF TECH CAMBRIDGE.

[21] M. Ashraf, J. Young, J.S. Lai et al. (2011). AIAA Journal, 49(7), 1374-1386 [22] V. Sousa, M. de M Anicezio, C. De Marqui Jr et al. (2011). *Enhanced aeroelastic energy harvesting by exploiting combined nonlinearities: theory and experiment*. Smart Materials and structures, 20(9) 094007

[23] M. Bryant, E. Garcia (2011). *Modeling and Testing of a Novel Aeroelastic Flutter Energy Harvester*. Journal of Vibration and Acoustics 133(1), 011010

[24] C. De Marqui, A. Erturk . *Electoaeroelastic analysis of airfoil-based wind energy harvesting using piezoelectric transduction and electromagnetic induction* (2012). Journal of intelligent materials and structures, 24(7), 846-854

[25] Taylor, G. W., Burns, J. R., Kammann, S. M., Powers, W. B., & Welsh, T. R. (2001). *The Energy Harvesting Eel : A Small Subsurface Ocean / River Power Generator*, 26(4), 539–547.

[26] Sirohi, J., & Mahadik, R. (2012). *Harvesting Wind Energy Using a Galloping Piezoelectric Beam*. Journal of Vibration and Acoustics, 134(1), 011009.

[27] Energy, H. W. LLC," Humdinger Wind Energy," 2009.

[28] Z. Peng, Q. Zhu (2009). *Energy harvesting through flow-induced oscillations of a foil*. Physics of fluids, 21(12), 123602

[29] Carr, L. W., McAlister, K. W., & McCroskey, W. J. (1977). Analysis of the development of dynamic stall based on oscillating airfoil experiments. NASA TN D-8382

[30] Richards, A. J. (2013). *Tuning the passive structural response of an oscillating-foil propulsion mechanism for improved thrust generation and efficiency* (Doctoral dissertation, University of Victoria).

[31] T. Kinsey, G. Dumas (2012). *Three- Dimensional effects on an oscillating-foil hydrokinetic turbine*. Journal of fluids engineering, 134(7), 071105

[32] Davids, S. T. (1999). *A computational and experimental investigation of a flutter generator* (Doctoral dissertation, Monterey, California: Naval Postgraduate School).

[33] Q. Xiao, Q. Zhu (2014). *A review of flow energy harvesters based on flapping foils*. Journal of fluids and structures, 46, 174-191

[34] M. Bryant, E. Wolff, E. Garcia (2011). *Aeroelastic flutter energy harvester design: the sensitivity of the driving instability to system parameters*. Journal of smart Materials and structures 20(12), 125017

[35] Field Calculator. (n.d.). Retrieved July 24, 2015, from https://www.kjmagnetics.com/fieldcalculator.asp

[36] F. Beer, E.R. Johnston, J. DeWolf (2005), *Mechanics of Materials (4th Edition)*. New York, NY: McGraw-Hill Irwin.

[37] McKinney, W., & DeLaurier, J. (1981). *Wingmill: an oscillating-wing windmill*. Journal of energy, 5(2), 109-115.

[38] Tacoma Narrows Bridge (1940). (n.d.). Retrieved July 24, 2015, from http://en.wikipedia.org/wiki/Tacoma_Narrows_Bridge_(1940)